Dual Mode Macro Fiber Composite-Actuated Morphing Tip Feathers for Controlling Small Unmanned Aircraft

Samuel Kim Rubenking

Thesis submitted to the Faculty of the

Virginia Polytechnic Institute and State University

in partial fulfillment of the requirements for the degree of

Master of Science

in

Aerospace Engineering

Kevin B. Kochersberger, Chair

Michael K. Philen

Gary D. Seidel

May 4, 2017

Blacksburg, Virginia

Keywords: Macro Fiber Composites, Proverse Yaw, Induced Drag, Artificial Feather, Smart Materials

Dual Mode Macro Fiber Composite-Actuated Morphing Tip Feathers for Controlling Small Unmanned Aircraft

Samuel K. Rubenking

Abstract

The transition of flight from manned to unmanned systems has led to new research and applications of technology within the field that, until recently, were previously thought to be unfeasible. The industry has become interested in alternative control surfaces and uses for smart materials. A Macro Fiber Composite (MFC), a smart material, takes advantage of the piezoelectric effect and provides an attractive alternative actuator to servos in the Small Unmanned Aerial Systems (SUAS) regime of flight. This research looks to take MFC actuated control surfaces one step further by pulling inspiration from and avian flight. A dual mode control surface, created by applying two sets of two MFCs to patch of carbon fiber, can mimic the tip feathers of a bird. This actuator was modeled both using Finite Element Analysis (FEA) and Computational Fluid Dynamics (CFD). Real-world static testing on a feather confirmed preliminary FEA results, and wind tunnel tests simulating assumed cruise conditions confirmed the feather would not exhibit any adverse structural behaviors, such as flutter or aeroelastic divergence. From its modeled performance on a wing using CFD, the MFC feather proved to be a success. It was able to produce a wing that, when compared to a traditional rectangular wing, yielded 73% less induced drag and generated proverse yaw. However, the MFC feathers alone, in the configuration tested, did not produce enough roll authority to feasibly control an aircraft.

Dual Mode Macro Fiber Composite-Actuated Morphing Tip Feathers for Controlling Small Unmanned Aircraft

Samuel K. Rubenking

General Abstract

The transition of flight from manned to unmanned systems has led to new research and applications of technology within the field that, until recently, were previously thought to be unfeasible. The industry has become interested in alternative control surfaces and uses for smart materials. A Macro Fiber Composite (MFC), a smart material, takes advantage of a specific material property and provides an attractive alternative actuator to servos in the Small Unmanned Aerial Systems (SUAS) regime of flight. This research looks to take MFC actuated control surfaces one step further by pulling inspiration from and avian flight. A dual mode control surface, created by applying two sets of two MFCs to patch of carbon fiber, can mimic the tip feathers of a bird. This actuator was modeled both using Finite Element Analysis (FEA) and Computational Fluid Dynamics (CFD). Real-world static testing on a feather confirmed preliminary FEA results, and wind tunnel tests simulating assumed cruise conditions confirmed the feather would not exhibit any adverse structural behaviors, such as flutter or aeroelastic divergence. From its modeled performance on a wing using CFD, the MFC feather proved to be a success. It was able to produce a wing that, when compared to a traditional rectangular wing, yielded 73% less induced drag and generated proverse yaw. However, the MFC feathers alone, in the configuration tested, did not produce enough roll authority to feasibly control an aircraft.

Acknowledgments

This research would not have been possible without the support of those closest to me. First, I would like to thank my parents, Brian and Debbie Rubenking, and my sister, Alison. Without their encouragement and love I would not have found my way. Their support enabled me to find the strength to keep pushing forward.

I am grateful to my adviser, Dr. Kevin Kochersberger, for this amazing opportunity that has allowed me to conduct the type of research in which I am most interested. He not only gave me the chance to conduct this research but aided me innumerable times along the way. Dr. Kochersberger guided me through an introduction to smart materials and interactions with my company sponsor. From the courses he recommended to me, I learned many valuable skills beneficial to both my research and applications in my field outside of academia. Lastly, he taught me time management and how to lead multiple projects, which I will take with me the rest of my life.

I would also like to thank my sponsoring company, Prioria Robotics. They not only helped to fund the research, but also helped to push the research forward and direct the research goals. Meetings with Prioria always brought new insight to the research and gave me inspiration to explore new paths. I would like to specifically acknowledge Mujahid Abdulrahim. As project lead, he helped to manage the research and gave me good feedback on my work.

Finally, I would like to thank my fellow lab mates. Their support and motivation was priceless. Specifically, thanks go to Joshua Eddy without whom I would not have been able to complete the

research in time. Thank you also to Zachary Standridge and Andrew Morgan for their teaching and guidance in the manufacturing processes necessary for the research.

Contents

List of Figures

List of Tables

Chapter 1

Introduction

Quickly growing in popularity, the Small Unmanned Aerial Systems (SUAS) market has caused a large upheaval in the aerospace research community, shifting the focus from large manned aircraft like that of a Boeing 747 or even a Cessna 172 to SUAS, like that of a multirotor or a backpackable fixed wing craft. These unmanned systems are the future of aviation and possess far reaching applications both in and outside the field. Improvements on SUAS, depending on the focus, can transfer to much larger unmanned systems, so while the field itself is quite broad, the scope of the work described in this thesis focuses on miniature Unmanned Aerial Vehicles (UAVs). Unlike the popularized US predator, miniature UAVs are classified under 55 lbs and can be used in a much broader range of missions.

Focusing on small fixed-wing unmanned vehicles allows this research to look into a relatively specific and under-represented solution to aircraft control, the Macro Fiber Composite (MFC). While the MFC represents a relatively new and versatile technology, even when restricted to the field of aviation, his research investigated its use in control surface actuation. Traditionally, fixed-wing aircraft control their roll rates and bank angles using small flaps (ailerons) on the outboard sections of a main wing. These ailerons asymmetrically change the lift produced by each half span of the wing causing the plane to rotate along its longitudinal axis. However, this traditional design of an aircraft wing has a number of significant drawbacks, which this thesis

will explore.

1.1 Motivation

The motivation behind the research documented in this thesis was to study and evaluate the feasibility of implementing MFC-actuated feathers to control and/or improve the flight characteristics of SUAS. The use of MFCs as a means to control miniature aircraft has been touched upon only lightly in the academic field; however, the technology has been studied only under the purview of wing camber control. Furthermore, all previous studies have been conducted using a single mode of actuation on a lifting surface. Most notably, see the building research of Onur Bilgen, [9], and then Eric Gustafson, [11], both of whom looked to construct a small fixed-wing aircraft that implemented thin flexible wings morphed by MFCs. Later that research was expanded upon by Troy Probst, [13], who morphed thick airfoils using MFCs. While these forays into the field shed light on the possible benefits over servos, their results were little more an extension of conventional control means.

This research looks to expand on the possible uses of the MFC in controls and aerodynamics by leveraging the advantages defined by the previous work. The following will utilize the thin nature of the MFC by using them as the control surface itself. The use of these control surfaces as feathers allows for bimodal actuation, twisting and bending, possibly giving an aircraft greater endurance and maneuverability. Experiments and simulations were run during the course of this research to determine the ability of such an approach to aircraft control.

1.2 Organization

The research described in this thesis follows three main paths: first, the design of the MFC control surface using past research and analysis tools; second, the testing of said control surface

to confirm analysis; and finally, to simulate its use on a wing to analyze its range of usability. The first section of the research looks at analyzing the actuation of the MFCs on thin composite materials using a finite element analysis (FEA) program. This was then used to give a preliminary understanding of what type of morphing could be expected when MFCs were applied in a bimodal morphing structure. The second section builds off the first, and applies the model to a real world test article. Static tests on the article attempted to verify the computational results, and wind tunnel testing on the article helped to show critical aerodynamic properties of the control surface. The final section works off the wind tunnel testing using computational fluid dynamics (CFD) to ascertain the effectiveness of the feather as a viable control surface or as a means to increase efficiency during flight.

Chapter 2

Literature Review

This section describes, briefly, the prior work and technology that this research expands. The review of this work comes in five sections. The first is an overview of MFCs as a technology and how they operate. The second summarizes basic aircraft controls as they pertain to the MFC control surfaces. The third section reviews a few of the existing aerial control systems that implement MFCs as actuators. Finally, the last two sections describe the analysis tools used throughout the research in this thesis.

2.1 Macro Fiber Composites

Macro Fiber Composites (MFCs), were created and published by NASA. "[MFC] was developed as a precision manufactured, lower-cost alternative to early generation piezoelectric fiber composite devices" ([14]). The MFC was invented in 1996 and the second generation refinement came out in 2003. Smart Material Corp. is now the distributor for the patented technology ([2]).

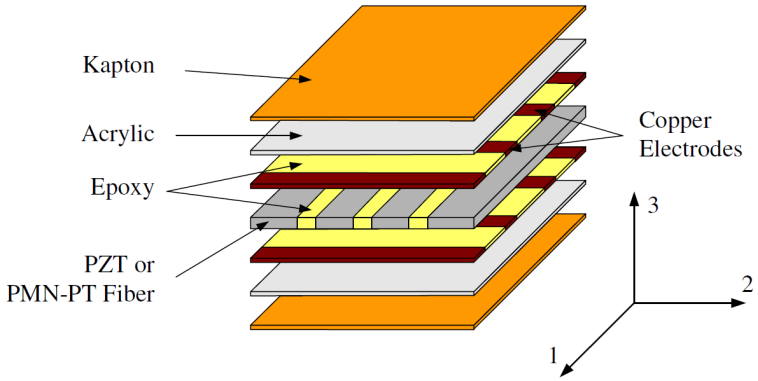

Figure 2.1: Composite layup of an MFC ([1])

Piezoelectric materials are the active smart material that drives the MFC. The piezoelectric material used in the MFC is a PZT fiber which is a special type of ceramic fiber. The MFC is a composite actuator that is created by sandwiching the PZT fibers between two copper electrodes and surrounding that with acrylic and Kapton. Fibers are set in an epoxy matrix which is used as the bonding agent for the composite and keeps the PZT fibers aligned to the desired orientation. Surrounding the PZT and electrodes, the Kapton and acrylic sheets protect and insulate the actuator from the elements (Figure 2.1).

The MFCs construction, documented thoroughly in [14], shows a layering of orthotropic materials from the PZT fiber and epoxy, to the copper electrodes and Kapton. This layup style means that the material properties of the MFC can be accurately calculated using lamination theory. Examples can be seen in equation 2.1 where E and G are the Young's and shear modulus respectively, ν is Poissons ratios, and m and f represent the matrix and fiber respectively ([1]).

$$\begin{aligned} E_1 &= E_{1_f} V_f + E_m V_m \qquad & E_2 &= \frac{E_{2_f} E_m}{E_{2_f} V_m + E_m V_m} \\ G_{12} &= \frac{G_{12_f} G_m}{G_{12_f} V_m + G_m V_f} \qquad & \nu_{12} &= \nu_{12_f} V_f + \nu_m V_m \end{aligned} \tag{2.1}$$

The MFC as an actuator generates strain through its electromechanical properties derived in [1].

The results are summarized by equations 2.2 and 2.3. While the MFCs used to be driven by the non-principal piezoelectric constant d_{13} the latest refresh on the actuators uses the principal d_{33} effect. This allows the MFC to generate much larger strains on the order of 1000ppm. This large strain, coupled with significantly higher strain energy than traditional piezoceramics, makes the MFC an attractive smart material actuator.

$$d_{33}^{\text{eff}} = \frac{d_{33}^{p}}{1 + \frac{V_2^m}{V_2^p}\frac{E_m}{E_{3_p}}} \tag{2.2}$$

$$d_{31}^{\text{eff}} = V_p^2 d_{31}^{p} \tag{2.3}$$

For material layups like the MFC, the behavior of the piezoelectric effect can then be defined using the equation 2.4, shown below. Note that T represents mechanical stress, s^E is mechanical compliance, S is total strain, and E is the electric field applied. From this stress-strain equation, the entire MFC layup strain field may be solved ([15]).

$$S_{ij} = s_{ijkl}^{E} T_{kl} + d_{kij} E_k \tag{2.4}$$

The strain generated by MFC patches is on the order of 0.1 percent of the total length. Therefore, by themselves, they show little promise of being used as actuators. However, when attached to a host material in a layup, large amounts of strain energy can be transferred, generating much larger deflections through bending and twisting (Figure 2.2).

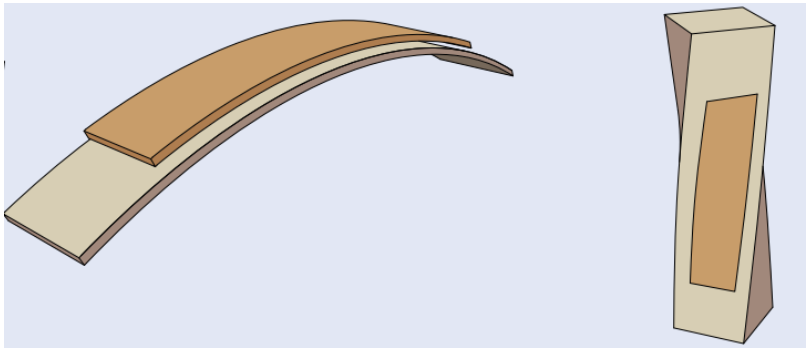

Figure 2.2: MFC with host material deflection modes ([2])

These deflections of host material are generated using a 0° fiber orientation with respect to the longitudinal axis for the bending mode and 45° for the twisting mode. Both of these deflections can be magnified by creating a bimorph, which is a sandwiching of the host material with two MFCs in which the MFCs will counter-actuate. An example of this for the bending mode can be seen in Figure 2.3. These bimorphs are just one way that MFCs can be implemented as an actuator in a control system (discussed further in section 2.3).

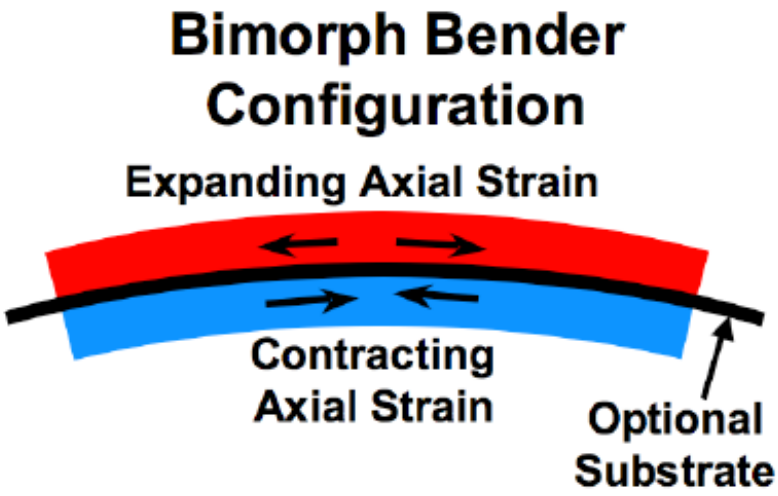

Figure 2.3: MFC bending bimorph example [3]

A full list of MFC properties was provided by the manufacturer Smart-Material Corp. and can be found in Table 2.1 ([2]).

Table 2.1: MFC Properties

Properties	**Value**
Free-strain per volt for d_{33}	0.9 ppm/V
Maximum operational positive voltage	+1500 V
Maximum operational negative voltage	-500 V
Tensile modulus, E_1	30.336 GPa
Tensile modulus, E_2	15.857 GPa
Poisson ratio, ν_{12}	0.31
Shear modulus, G_{12}	5.515 GPa
Density, ρ	5.44 g/cm^3
Thickness, t	0.3 mm

2.2 Aircraft Controllability

Since the creation of the aircraft by the Wright bothers, man has tried to solve the problem of coordinated flight and inefficiency. Coordinated flight is described, for an aircraft, as a maneuver, such as a turn, where the aircraft is rolled, i.e banked, while yawing such that the aircraft flies with zero sideslip. Rolling of an aircraft is the rotation of the vehicle about its longitudinal axis, the line directed straight out the nose of the plane, most often in the direction of travel. Yaw is the rotation of the plane about the vertical axis, the line directed out the belly of the aircraft most often toward the ground. The axis system described here is also known as the body axis system. Finally, sideslip is any portion of the aircraft's wind velocity projected on the plane created by the lateral axis and longitudinal axis not directed in the longitudinal axis direction (Figure 2.4) ([4]).

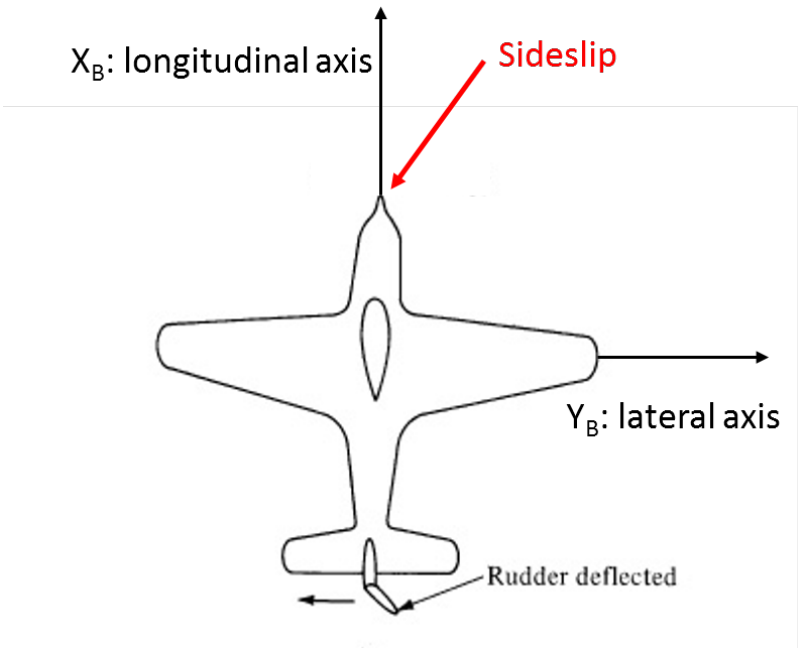

Figure 2.4: Description of sideslip ([4])

The need for a tail on some aircraft such as the Wright Flier comes form the control phenomenon known as adverse yaw. Adverse yaw occurs when an aircraft rolls one direction using its ailerons, small flaps that change the lift of the portion of the wing, causing the aircraft to yaw in the opposite direction. So for example if the airplane were to roll into a right hand turn the airplane would start to yaw to the left. This phenomenon occurs due to the aerodynamic principle induced drag. Induced drag is the portion of drag that is directly caused by lift, so increased lift means increased drag. To roll a plane one side of the wing must produce more lift than the other, inducing a moment about the X_B axis. This causes an imbalance in induced drag on the wing causing the adverse yaw (Figure 2.5). This has been counteracted with the introduction of a vertical tail which will cause horizontal lift to control the yaw of the plane. The addition of a tail can be very detrimental to an aircraft adding both weight and drag ([4]).

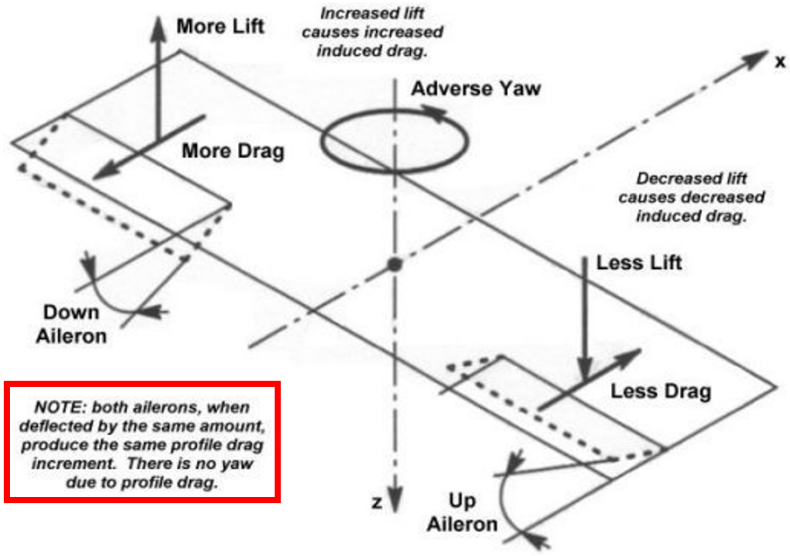

Figure 2.5: Description of adverse yaw ([4])

What was believed to be the best wing loading distribution for an airplane, elliptic, allows for the greatest lift to be generated given a certain wing area and span.[16] This wing loading distribution has been used for many a year on many an aircraft, however it has one large flaw. Elliptic wing loading is one of the reasons for adverse yaw. Believed for a while to be a necessary evil, adverse yaw is not inherent to winged flight, one only has to look nature's solution, birds. Birds fly without a vertical stabilizer and are perfectly capable of executing coordinated turns. As it turns out birds employ a wing loading with a bell shape (see Figure 2.6). This bell shape is the wing loading shape that minimizes induced drag for a given amount of lift ([5]).

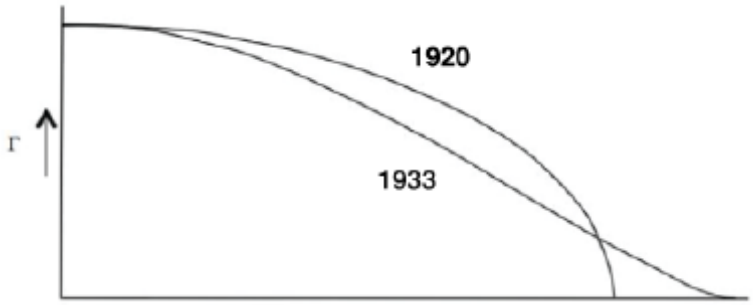

Figure 2.6: Wing loading for maximum lift (1920) and minimum induced drag (1933) ([5])

Not only does the bell shaped wing loading decrease the amount of induced drag, it also has the advantageous property of proverse yaw. Proverse yaw is the opposite of adverse yaw where rolling in one direction causes yaw in the same direction. This is how birds can fly without vertical stabilizers. The effect occurs by twisting the outboard section of the wing such that it produces zero lift at the tip. The vorticies shed by the wing cause an upwash on the outboard wing. This upwash generates induced thrust, induced drag in the direction of flight. By reversing the direction of induced drag a the tip of the wings the aircraft or bird can exhibit proverse yaw (Figure 2.7) ([5]).

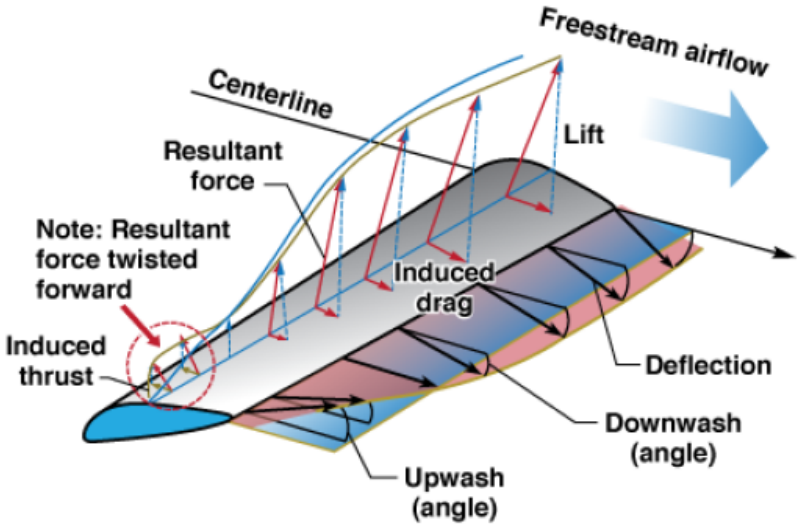

Figure 2.7: Proverse yaw with bell shaped spanloading ([5])

This aerodynamic phenomenon, proverse yaw will be the topic of interest regarding the MFC feathers discussed in this thesis. The objective of the feathers is to exhibit proverse yaw when implemented on a wing tip. The feathers will twist to change the wing tip camber producing a more efficient wing while maneuvering.

2.3 MFC Control Systems

While MFCs are a relatively new actuator technology, they have been around for over 20 years. Despite their many advantageous material properties, there have been relatively few published works on MFCs as actuators. However, in the field of aerospace, there have been a couple of recent works that showcase the MFCs potential for control systems in aerial vehicles. The applications are quite numerous, but this section will focus on just a few: camber control of a flapping flexible wing, twist control of a rotor blade, and aileron replacement for a UAV wing.

2.3.1 Camber of a Flapping Wing

A team in the Aerospace Department at the Korea Advanced Institute of Science and Technology (Daejeon, South Korea) has developed a smart flapping wing that mimics bird flight. It uses MFCs to change camber of a flexible wing during the different phases of flapping flight. By doing so the team has achieved an accurate bird-like motion that produces more thrust and lift than with uncontrolled wing camber (Figure 2.8). This change in camber allows for the flapping wing to take advantage of unsteady aerodynamics increasing lift compared to uncambered wings.

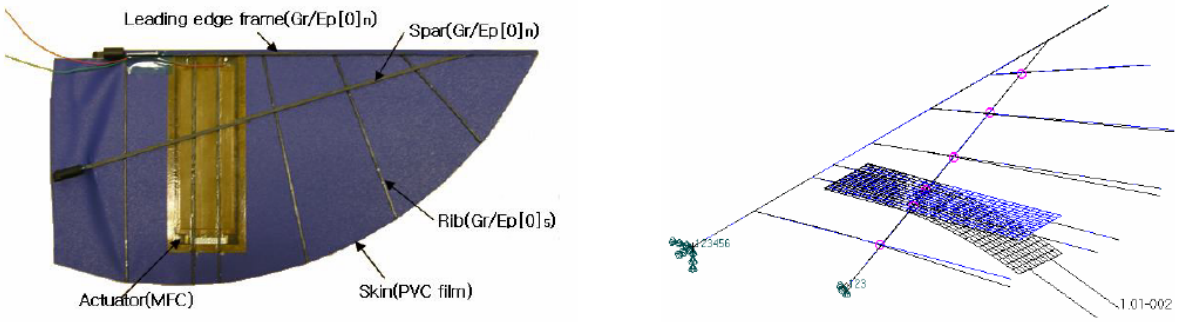

Figure 2.8: Left: smart wing, Right: Finite Element Analysis model ([6])

The Korean team modeled their wing using NASTRAN, a finite element analysis (FEA) tool, the same one used for this research ([6]). They implemented a piezoelectric to thermal analogy to

run test cases. This analogy translates the piezo-constant to a thermal constant because the two generate the same stress-strain field in a computational analysis. From their model, they found an encouraging -15 to 5 mm tip displacement of the MFC (Figure 2.9) ([7]).

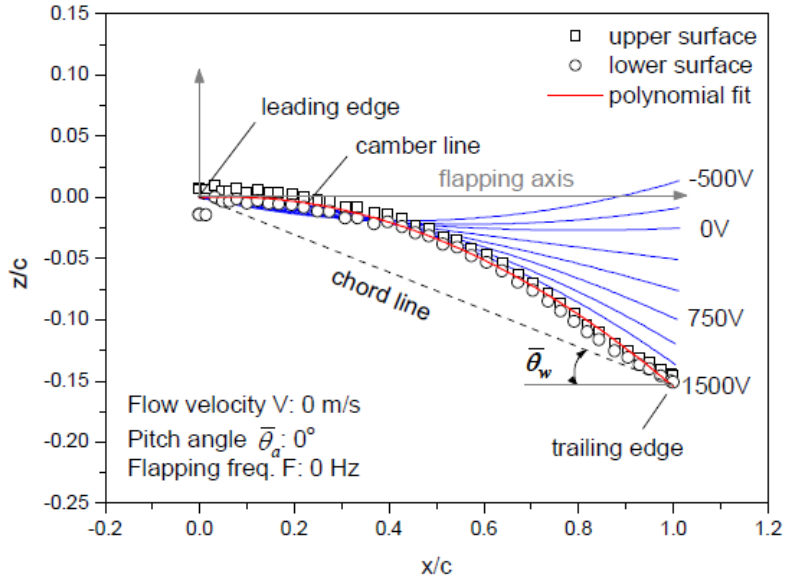

Figure 2.9: Flapping wing camber lines based on input voltage to MFC ([7])

This research shows great promise to use of the MFC for bending deflections and shows the accuracy of use of NASTRAN to model MFCs. This research has seen good results in use of the MFC as an actuator in a control system on wings even if these wings are not the same as the static wings of interest to this thesis.

2.3.2 Variable Twist of a Rotor Blade

Another project utilizing MFCs as actuators in the aerospace industry also originated from South Korea, this time from the School of Mechanical and Aerospace Engineering. A team there used the MFC in the 45° form to achieve active twist control across the span of a rotor blade. Specifically, in a 2005 paper [1], they studied the effectiveness of the single crystal MFC against other smart material devices. The research looked at the single crystal's rotational displacement

compared with a standard MFC and an anisotropic actuator, the Active Fiber Composite (AFC) developed by researchers at the Massachusetts Institute of Technology (MIT). The standard MFC is the type of actuator used throughout the research documented in this thesis.

The experiment described in the paper uses an ATR blade with a NACA0012 airfoil. It is constructed out of two layers of E-glass, both placed at 0° with respect to the blade axis. The blade has dimensions of 0.483 m for the radius and a constant chord length 0.05 m. The actuators are placed toward the leading edge of the blade (see Figure 2.10).

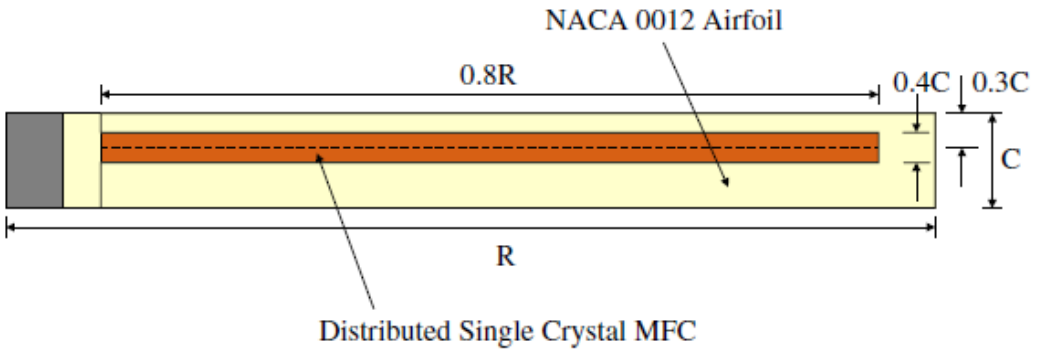

Figure 2.10: Rotor blade configuration ([1])

By driving all actuators to the same voltage, the team found that the single crystal MFC generated over double the tip twist compared to the standard MFC, and the standard MFC generated over twice the tip displacement as the AFC. The distribution of twist was a linear progression across the span (see Figure 2.11) due to the basic stress-strain relationship.

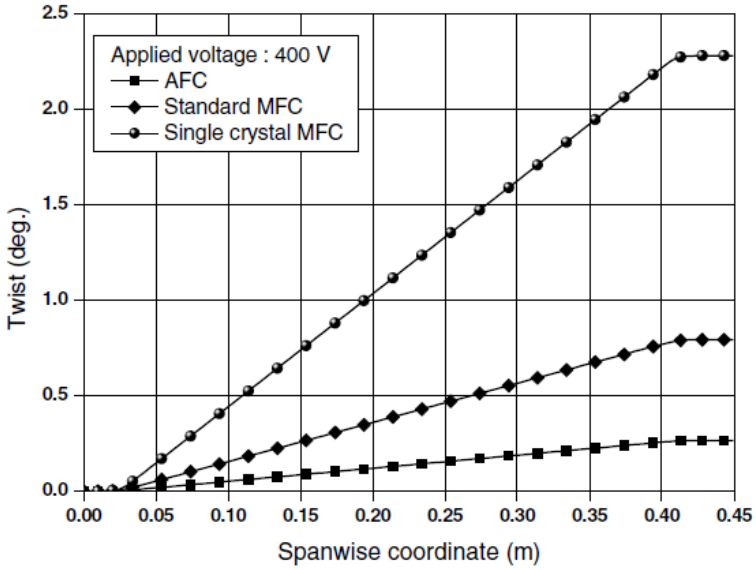

Figure 2.11: Twist distribution across blade span for applied 400V ([1])

These results show that while a single crystal MFC has better results than the other options, the standard MFC does show some potential as an actuator by still generating significant tip deflection. The single crystal MFCs have better performance than the traditional MFCs because they have lower stiffness and a larger piezoelectric effect. However, for aerospace applications, single crystal MFCs have a slightly higher density than the standard MFCs, meaning there is a performance/weight trade-off at any given size.

2.3.3 Aileron Replacement

The first significant writing on the topic of aileron and servo replacement that this research comes from the work done by Onur Bilgen in his thesis, [9]. His research documented the first wind tunnel test results on thick and thin MFC actuated airfoils were presented. The MFC actuated airfoil was then implemented and wind tunnel tested on an aerial vehicle. The research produced promising results in roll authority and lift control. The vehicle had wings made of three plies of fiberglass. The ailerons were controlled by MFCs that were in the layup between

two of the plies. The MFCs were 0° actuating and aligned parallel to the aircraft's longitudinal axis. This research would later be expanded upon by Eric Gustafson with a few alterations.

Building upon Bilgen's research, Gustafson's thesis, [11], models the MFC and host material using a thermal analogy in NASTRAN that will be closely followed in this thesis. The research applies the MFC to a cabon fiber GenMAV airfoil as a bimorph. Gustafson followed Bilgen in wind tunnel testing of the airfoil; however, he also built upon the aerodynamic data with an experiment on the MFC actuation limit cycle oscillations (LCO). This LCO occurs with certain flow induces vibrations that cause an extreme deformation due to the coupling of the aero-structural loading. It was found that this behavior only becomes a problem at large aerodynamic loads. This will not affect the MFC feathers used in this experiment, as they are to be implemented as wing tip feathers. At the wing tips, aerodynamic lift drops to zero. Therefore, the extreme aerodynamic loading experienced by the feathers should never be a factor.

The next in the research line for implementing MFCs for aircraft control is Troy Probst. His thesis, [13], gave more insight to the MFC's control response in direct comparison to a servo. Probst used MFC bimorphs to drive a thick airfoil's trailing edge, thereby mimicking a traditional aileron or flap. The benefit of using the MFCs was the continuous nature of the airfoil with no moving mechanical parts. The most notable result was that, even at load, phase lag of the actuator remained relatively unaffected. Also, MFCs demonstrated a better control behavior than servos at higher frequencies and could allow for larger bandwidth than a traditional servo. Probst was the first in this line of research to use the MFCs at a different angle relative to the wing geometry. By placing the MFC at a 45° angle to the chord, Probst was able to twist the wing along its span. Documented in a paper, [17], Probst showed that, while unable to match the magnitude of roll moments generated by traditional servos, the MFC twisting wing demonstrated a faster response. This MFC application was implemented on a thin wing and shows for use in twist and flight controlling actuator, the MFC makes a more than adequate candidate.

2.4 Bird Flight

This research looks to implement MFCs as actuators on wing tip feathers, mimicking the function feathers have in avian flight. Birds, as discussed earlier, exhibit the useful aerodynamic characteristic of proverse yaw. However, birds also flap their wings to generate lift and thrust, a mode that will not be available to the models designed in this thesis. To limit the scope of this paper, this review will focus mainly on a bird of prey, specifically, the eagle, because eagles spend most of their flying time soaring rather than flapping. From an exhaustive study done on bird wing shape, it was found that eagles like other large birds of prey have large rectangular wings for their overall mass ([18]).

Bird wing tip feathers have a few interesting properties: they can act as winglets that reduce induced drag (Figure 2.12 and the wing tip feathers change how the vorticies shed by the wing interact with the outboard wing. The decrease in induced drag is the same effect seen in the induced drag of the bell-shaped lift distribution described in [5]. In some tests the feathers reduce the induced drag by over 50%. Because of this decrease in drag, slotted wing tips can generate significantly higher lift to drag ratios (L/D), which is the main characteristic determining an aircraft's endurance ([8]).

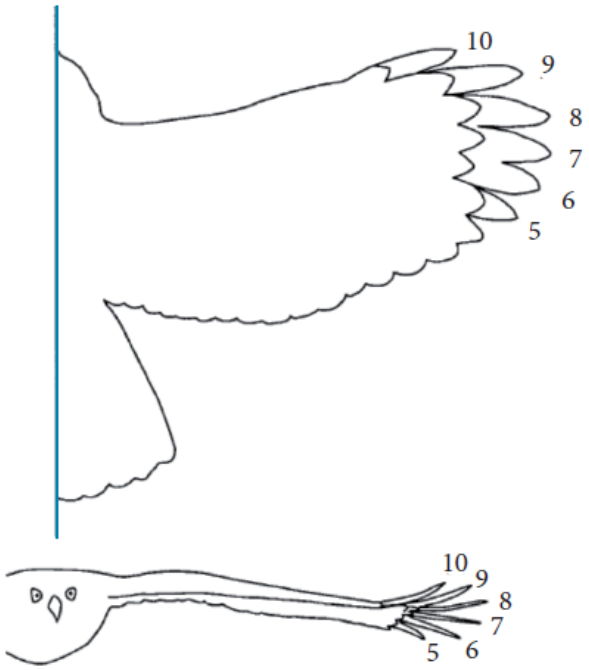

Figure 2.12: Wing tip feathers of a Harris' Hawk ([8])

Another advantage to bird's bell-shaped wing loading is a reduction in structural weight. Because the lift generated out at the tips of the wings falls to zero gradually, light flexible feathers can be used, as they do not carry high aero-loads. Most of the lift is generated on the inboard section of the wing. This means the outboard section can be substantially lightened as it experiences lower bending moments compared to an elliptic loading. While engineers have been creating aircraft optimized for wing loading efficiency, birds have optimized for a structural and control efficiency. Lastly, because of their unique wing loading, bird wings do not exhibit wingtip stall like the swept wings of traditional aircraft ([5]). The MFC feather created in this thesis looks to mimic birds in order to gain their advantageous aerodynamic and structural characteristics while applying them to SUAS.

2.5 Finite Element Analysis

The structural modeling done in the research for this thesis was conducted using Femap, a NASTRAN pre- and post-processor. Femap, created by Siemens Product Lifecycle Management Software Inc., does no actual structural computations; it just generates NASTRAN input files and reads in NASTRAN results. Femap does, however, aid in the creation of structural models as well as the parsing of results into a more readable form. NASTRAN, standing for NASA Structural Analysis, was developed in the 1970s as a finite element analysis tool. Due to its early birth, the entire data entry and results are text based. For this reason, Femap uses a graphical user interface to allow for data interaction via plots and graphs. Despite its old roots, Nastan is one of the top analytic solvers in industry and generates high fidelity FEA ([19]). Following several approaches mentioned earlier, Femap was used, along with the piezoelectric thermal analogy, to model the MFC actuation.

2.6 Computational Flow Dynamics

To evaluate the aerodynamic characteristics of a wing using the wing tip feathers an analysis tool, the open source Matlab Tornado code, was chosen. This code uses a vortex lattice method to calculate aerodynamic loads on lifting bodies. Tornado uses wing properties: span, chord length, twist, and airfoil, to name a few, to generate panels that to represent the wing. Panels lie on the chord line and take the slope of the mean camber line of the wing a the panels center point. Each panel has a horseshoe vortex line extending down stream and coming around the quarter chord of the panel. The program solves the vortex strengths of each panel by applying a no flow condition at each panels collocation point at 3/4 chord. Once the vortex strengths have been calculated the aerodynamic forces on the lifting bodies become trivial. Because the vortex panel method assumes invicid flow it cannot take into account viscous effects. However,

Tornado can calculate induced drag, or drag generated by lift. This is essential in determining the desired proverse yaw effect ([20]).

Chapter 3

Finite Element Analysis of a Macro Fiber Composite Feather

This section will look at the finite element analysis completed to model MFCs as actuators on flexible wing tip feathers for SUAS. This modeling implemented the piezoelectric to thermal analogy to simulate the piezoelectric effect. All modeling was done using Femap as a pre- and post-processor to NX NASTRAN.

3.1 Model Development

To develop the model of the MFC feather, the initial starting point was the research previously done by Eric Gustafson, [11]. This set up a plate element in Nastran to represent the composite layup, including the host material and MFCs. While this worked well when processed directly with NASTRAN, the Femap pre-processor would not allow true thickness to be applied to the composite layup. This was due to the finite element used by the plate element chosen. The MFC layers had no lever arm to apply strain, so the two MFCs were essentially applying counter acting strains at the same mid-plane of the feather. To accommodate for this, a solid element was chosen to model the host material. This allowed plate elements representing the MFCs to

operate with a lever arm to the mid-plane (Figure 3.1). This model accurately depicts the active section being slightly smaller than the MFC patch and feather. However, in the initial study the feather was shrunk to fit the active section for ease of modeling. The bezels of inactive sections vary between sizes of MFC making consistent modeling overly difficult.

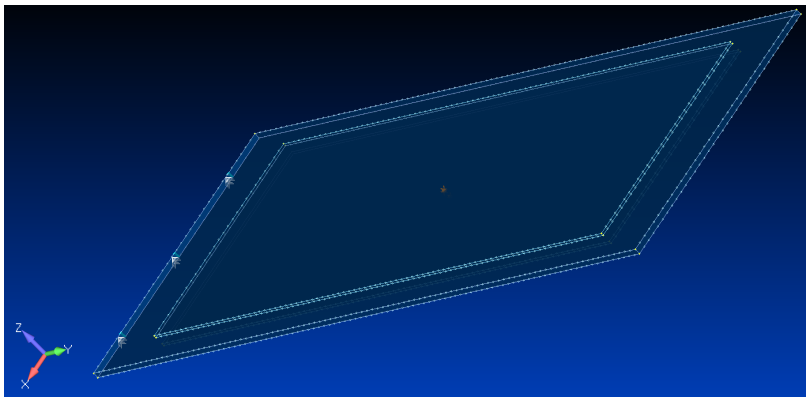

Figure 3.1: Sample Feather FEA Model with two MFC bimorphs

Figure 3.1 shows two sets of plates sandwiching the host material. These plates represent the active area of the MFC and lie at the patch's calculated mid-plane. This model is made up of purely geometric objects and any type of material (and material properties) can be applied to each. This allows for rapid analysis and development for future trade studies to be preformed.

From Gustafson's thesis, [11], the MFCs thermal expansion coefficients were used (equation 3.1). These transfer the voltage to temperature change one-to-one. Unlike the previous work, Femap allows placement of temperature changes on different regions easily, so adjustment for different voltages on separate MFC did not require changes in thermal expansion coefficients. This follows the analog to the piezoelectric effect discussed earlier (equation 2.4), with the equation 3.2.

$$\begin{bmatrix} \alpha_x \\ \alpha_y \end{bmatrix} = \begin{bmatrix} \frac{d_{31}}{\Delta_{el}} \\ \frac{d_{33}}{\Delta_{el}} \end{bmatrix} = \begin{bmatrix} -3.704 * 10^{-7} V^{-1} \\ 8.7 * 10^{-7} V^{-1} \end{bmatrix} \tag{3.1}$$

$$D = dT - \varepsilon E \tag{3.2}$$

3.2 Material Trade Study

The next step in the analysis of the MFC feather was to pick a host material. In order to accomplish the task, a trade study was conducted on the following properties: chord length, thickness, and Young's modulus. The ranges for each property may be found in table 3.1. The increment for Young's modulus was undefined because it was tested at leading 1 and 3 for each magnitude (e.g, 0.1 GPa, 0.3 GPa, and 1 GPa). The study looked at total tip rotational deformation in radians.

Table 3.1: Feather Properties

Properties	**Range**	**Increment**
Chord length	10-50 mm	10 mm
Thickness	0.1-0.5 mm	0.05 mm
Young's Modulus	0.1-300 GPa	NA
Poisson's Ratio	0.3	None
Span	100 mm	None

The trade study only measured rotation and included only one bimorph. Bending was ignored because studies had already been run looking at the effect of material properties like thickness on tip displacement. Postulating from prior work (Figure 3.2) tip deflection should increase with thinner host material (to a point), lower stiffness, and be independent of chord length. For this specific trade study, the shear modulus was not included as an independent variable because the Poisson ratio was fixed, thereby fixing the shear modulus given any specific value for Young's modulus.

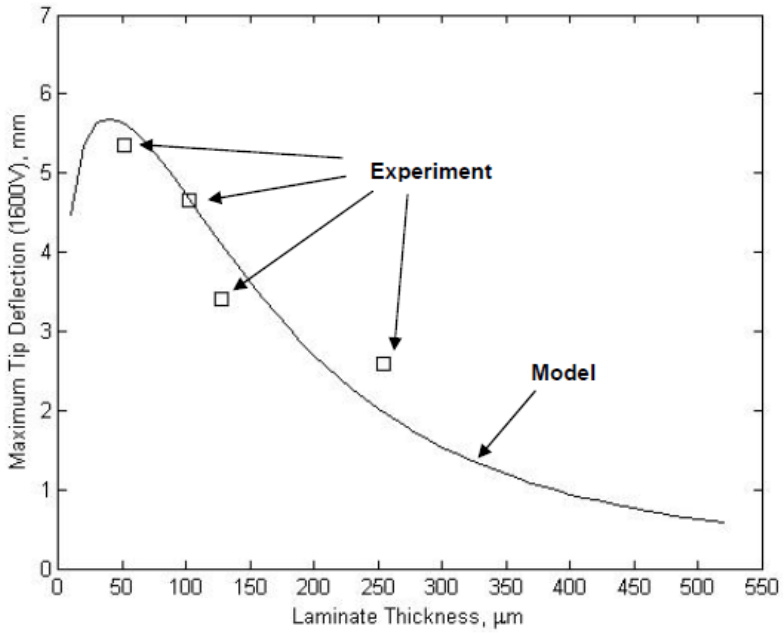

Figure 3.2: Bending tip deflection as a function of host material thickness ([9])

3.2.1 Constant Chord Length

The first result shows the radial displacement at the tip of the feather given a constant chord length. The study varies both the thickness and the Young's modulus. The results have been plotted in Figure 3.3. This plot completely encapsulates the general relationships for all chord lengths of interest. First, the plot shows that by increasing thickness, the total tip displacement decreases. This follows the thought that since increasing thickness increases the cross-sectional area and the torsional constant, (equations 3.3 and 3.4). For these equations b and a are the base and height of the cross section respectively, l is the length of the beam, G is the shear modulus, J is the torsional constant, and T is the torque applied. While there was no torque applied, stress was induced from strain generated by the MFCs, so it still holds that the twist decreases with increased torsional constant.

$$J \approx ab^3\left(\frac{1}{3} - 0.21\frac{b}{a}\left(1 - \frac{b^4}{12a^4}\right)\right) \tag{3.3}$$

$$\phi = \frac{Tl}{GJ_T} \tag{3.4}$$

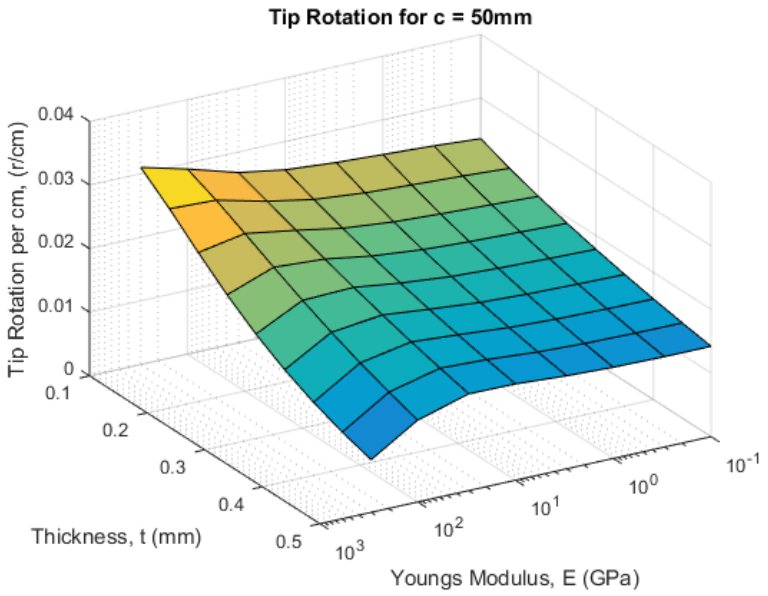

Figure 3.3: Twist tip deflection in radians given Young's modulus and thickness

Looking at Figure 3.3, the Young's modulus does not affect the tip displacement in the way it was initially thought. At low tensile stiffness, increasing Young's modulus actually increases tip displacement for thicker substrates. While no complete study was run on this unexpected effect, there may be some easy physical explanation. For any given run the strain energy imparted to the system by the MFCs was the same. The only thing changing was how the energy was dissipated through the material (see Equation 3.5).([1])

$$\delta U - \delta W_e x t = 0 \tag{3.5}$$

There were two main ways of deflection that the strain energy could be dissipated, twisting and

extension. The degree to which the material twisted relied on the materials torsional stiffness, GJ, while the extension relied on the material's axial stiffness, EA, where A is a cross sectional area. So the theory as to why twisting increases with Young's modulus at high thicknesses is that the ratio between EA and GJ changes such that more strain energy is dissipated through twisting deformation than through extension deformation.

3.2.2 Constant Young's Modulus

The next part of the trade study looked at the effects of chord length and thickness while holding Young's modulus constant. This study (Figure 3.4) exhibited much more predictable results. The thickness shows an inverse relationship to deflection as seen in the last section. Chord length has a linearly indirect effect on the tip deflection, but it could be said to be relatively constant and negligible compared to the effect of thickness. Figure 3.4 is quite representative of the behavior between chord length and thickness for all cases studied.

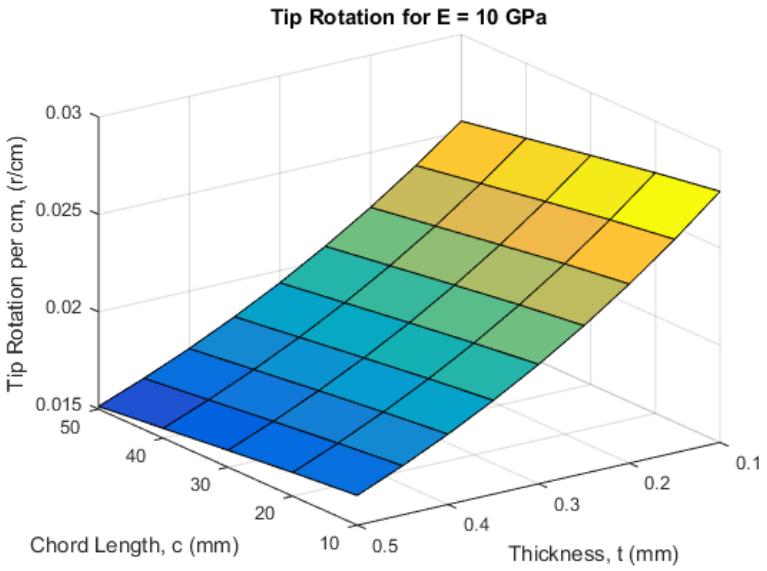

Figure 3.4: Twist tip deflection in radians given thickness and chord length

3.2.3 Constant Host Thickness

The final and most interesting case examined was the effect of chord length and Young's modulus on tip rotation, holding thickness constant. The results have been plotted in Figure 3.5. This again shows the interesting effect of Young's modulus increasing the tip rotation to a point, around 100 GPa, and then decreasing. This non-linear non-constant effect spans across all chord lengths tested. The chord length's effect is again minimal and linear, increasing the tip rotation indirectly with chord length. This relationship holds until the Young's modulus decreases below 10 GPa. Like the interaction with stiffness, the departure from linearity experienced by chord length at extremely low stiffness can most likely be attributed to the changing of ratio between the article's stiffness, EA and GJ.

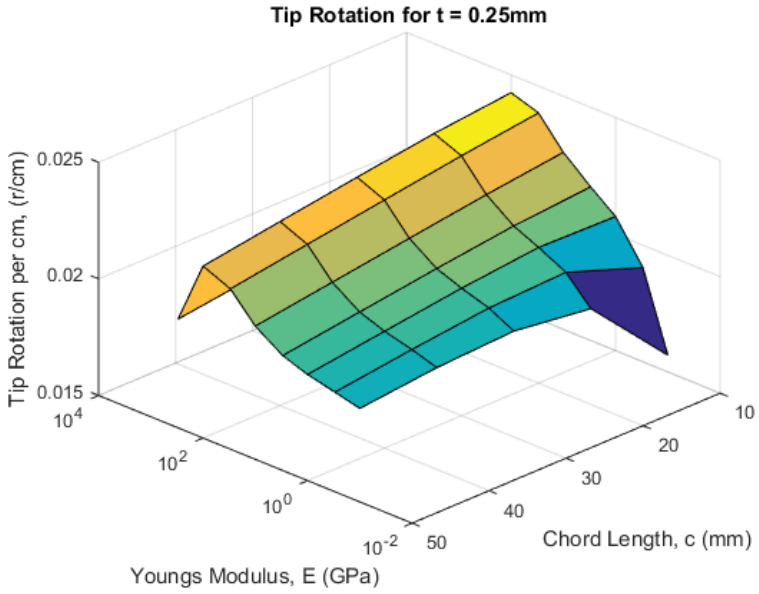

Figure 3.5: Twist tip deflection in radians given Young's modulus and chord length

3.2.4 Conclusions

From these trade studies on host material, it was determined that the optimal feather should have a relatively small chord length, be as thin as possible, and optimally have a Young's modulus

on the order of 100 GPa. These results do, however, have some caveats. The feather tested did not include realistic MFC shapes. The feathers were sized exactly to the MFC's active section, ignoring the typical bezels of non-active Kapton and acrylic. This means wide feathers may have better performance as there is a larger active to non-active area ratio on the MFC patch. Secondly, because the relationship between torsion and extension is still unknown the ranges of optimal Young's modulus may greatly depend on Poisson's ratio and other unknown factors. However, from the results the decision was made to further test two materials, carbon fiber and fiberglass, as candidates for a dual actuated feather. It was also decided that the MFCs used for the actuator would be the M8528-P1 and M8528-F1, 0° and 45° respectively. These both have active sections of 85 mm in length and 28 mm in width.

3.3 Bending Torsion Trade Study

Given that the two MFC patches had been picked, the size of the feather relative to model was now defined apart from thickness. The patches used had an overall length of 105 mm and a width of 35 mm with the patches centered both vertically and horizontally. They resembled Figure 3.1 with the inactive areas around the patch. A study was then conducted on the choices for host material: carbon fiber, and fiberglass, the material properties of which are displayed in Table 3.2.

Table 3.2: Host Material Properties ([12])

Material	**Density (g/cm^3)**	**E (GPa)**	**G (GPa)**	**Poisson's (Ratio)**
Carbon Fiber	1.6	70	5	0.1
E Fiberglass	1.9	25	4	0.2

The feather consists of a host material surrounded by two bimorphs. The MFCs were organized symmetrically about the host material that lies at the center. This means that the two bimorphs, one controlling bending the other controlling twisting, could either have been positioned on the

inside or outside. The convention used in this writing is to represent the bending bimorph with "B" and to represent the twisting with "T". They will be ordered starting with the inside going out, so "BT" represents a lay up of TBHBT (Twist, Bend, Host, Bend, Twist). Conversely, the label "TB" represents twisting as the inner bimorph and bending as the outer bimorph. This trade study examines the effect of thickness on the dual-mode deflection with both bending and torsion. To analyze this actuation, both the torsion MFCs and the top bending MFCs were set to 1500°C while the lower bending MFC was set to 500°C, which represents maximum deflection. Just like in the previous trade study, the tip deflections were recorded, bending in millimeters and twist in radians. The Figure 3.6 below shows the plotted results for the "BT" layup which compares the host materials, carbon fiber and fiberglass, against one another. Being significantly more flexible, fiberglass exhibits slightly larger deflections than the carbon fiber in both bending and twisting. However, as thickness increase the bending deflections for the two materials converge, but conversely, the twisting deflections diverge over the observed range.

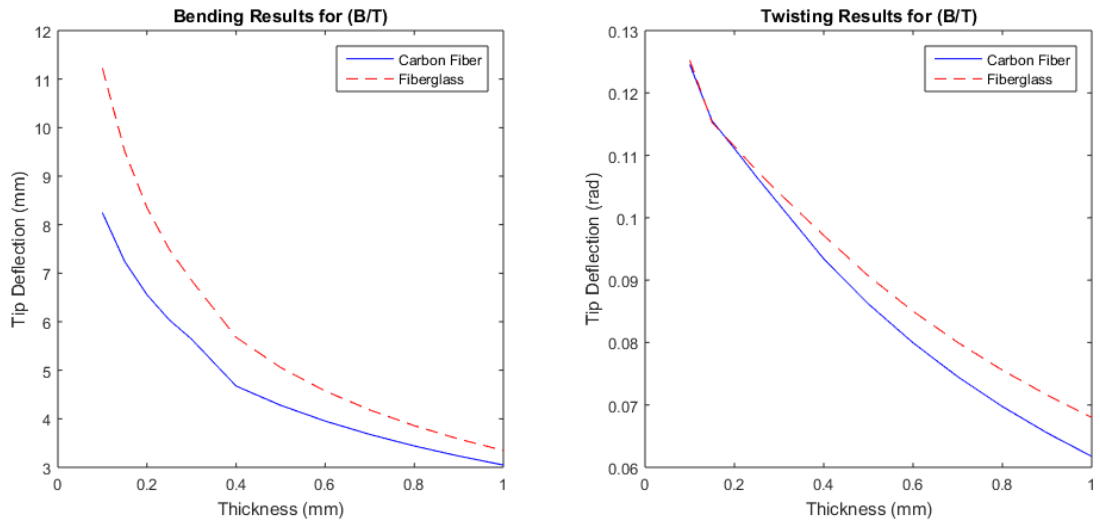

Figure 3.6: Tip deflection results for bending bimorph inside twisting bimorph outside (a) Bending deflection vs thickness, (b) Twisting deflection vs thickness

Interestingly, reversing the order of the MFC bimorphs significantly alters the results (see Figure 3.7). The bending deflections for the "TB" layup shows no real difference between carbon fiber

and fiberglass host materials for all tested thicknesses. The carbon fiber, this time however, has larger twisting deflections than the fiberglass for all thicknesses, the exact opposite from the previous "BT" layup. From these two figures, the decision was made to use carbon fiber as the host material. While slightly worse in the "BT" layup, small decreases in deflection magnitude was an allowable sacrifice for the added stiffness. The stiffness was thought to be necessary to avoid potential flutter of the feather at high speeds. This flutter and aeroelastic divergence would later be tested in Chapter 5. The displacement at extremely small thicknesses of the host material actually falls. This theoretical decrease in the displacement is not shown below because the thicknesses tested are not small enough.

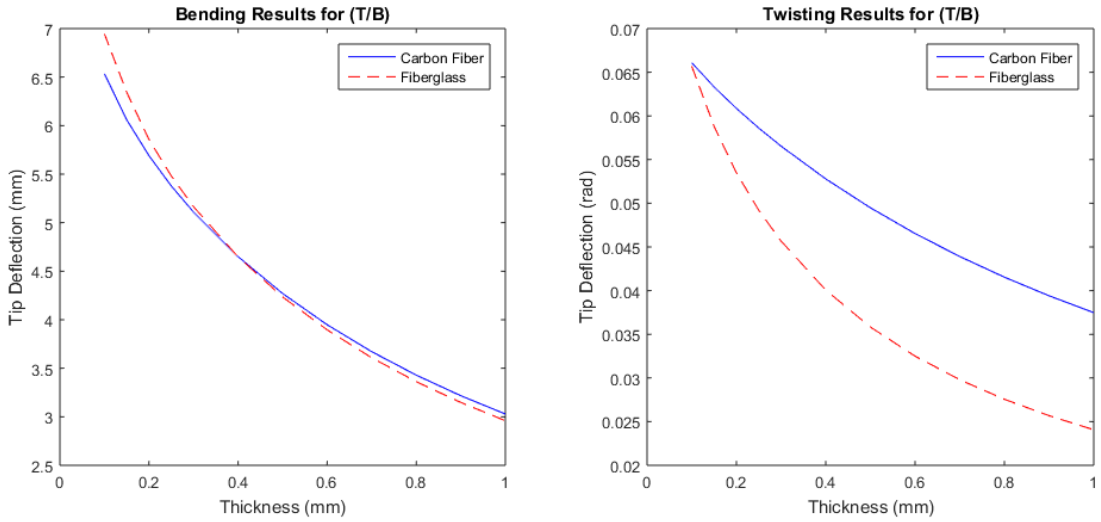

Figure 3.7: Tip deflection results for twisting bimorph inside bending bimorph outside (a) Bending deflection vs thickness, (b) Twisting deflection vs thickness

The final Figure 3.8 shows a comparison between the "BT" and "TB" layup schemes for the host material, carbon fiber. It is evident from the plots that the "BT" scheme performs equal to or better than the "TB" scheme in both deflection modes. So the feather's layup will be a carbon fiber host material with 0° MFCs as the inner bimorph and 45° MFCs as the outer bimorph.

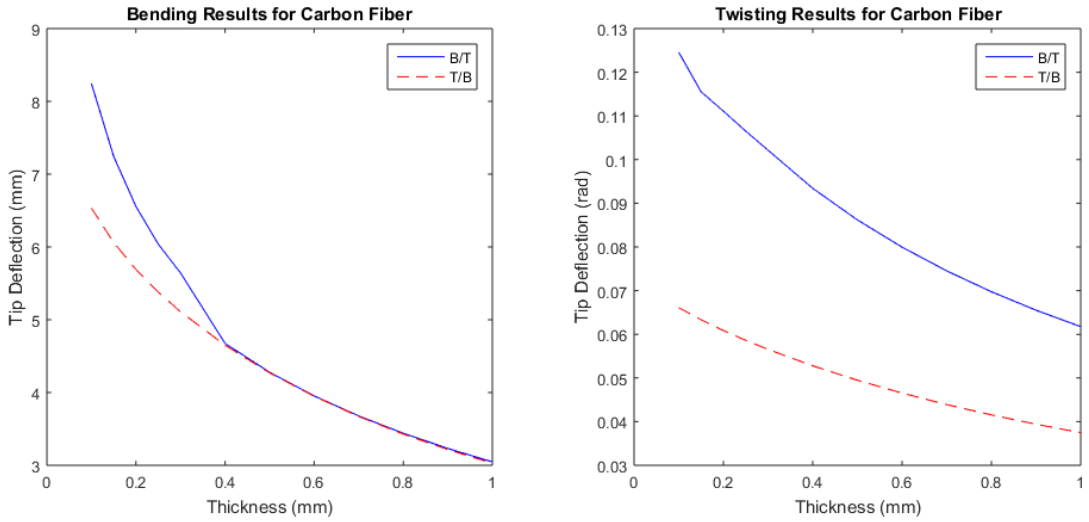

Figure 3.8: Tip deflection results for carbon fiber (a) Bending deflection vs thickness, (b) Twisting deflection vs thickness

In the previous Figure 3.8, the out-performance of the "TB" scheme by the "BT" scheme is most likely due to the physics of the strain generated by the MFCs. When it comes to the bending bimorph, the further from the center line the actuators lie the larger the lever arm and closer to the free strain the MFCs are able to achieve. However, because the MFCs are further from the center line, equal strain of the MFC induces a larger radius of curvature in the host material meaning a smaller deflection. So there is a trade off between lever arm and internal strain slope. In the range of thicknesses studied it is evident that the trade off between the two at thicknesses above 0.4 mm is negligible. So laying up the MFCs further from the center line has little to no effect on deflection. However, in the twisting results, it is evident that the distance from the center line, line of approximately zero strain, has a much larger effect on deflection magnitude than maximum strain experienced by the 45° MFCs. This difference is likely due to the difference in actuation angles between MFCs in the bimorph. The MFCs in the bending bimorph act in an anti-parallel direction to one another while MFCs in the twisting bimorph act perpendicularly to one another. Finally, the change in analysis interval at smaller thicknesses was an attempt to gain more granularity. And the departure from the smooth relationships at smaller thicknesses

seen in all plots stems from an inability to increase FEA fidelity past a certain point.

Chapter 4

Experimental Design

This chapter discusses the set up and construction of the MFC feather test article and rig used in both the static and wind tunnel testing. The materials and instrumentation required for the experiments is described in detail.

4.1 MFC Feather Construction

The construction of MFC feathers is a simple process if one is familiar with basic composite layup techniques. A list of the required tools and materials can be found in Table 4.1. The construction process involves laying up the feather in three phases, each involving the same steps. First, two pieces of woven carbon fiber fabric are attached using a mixture of the West resin and hardener. Both pieces of carbon fiber cloth will be lain up in the same 0° orientation. The layup is then transferred to a large section of Stretchlon. The Stretchlon, a vacuum bagging material, must be slightly larger than twice the layup area so that it may be folded over and sealed with the sealant tape to form the bag. However, pieces of peel ply and breather, both slightly larger than the layup, must first be placed over top of the article. Next, the bag valve must be inserted into what will be the topside of the bag. Finally, the bag may be closed and sealed with tape. The placement of the valve in the corner of the material in Figure 4.1. The hose, creating the vacuum, is then

far away from the portion of the layup that will be used as the host material for the test feather. This placement helps make sure that any epoxy pooling or material deformation caused by the vacuum does not affect the majority of the layup.

Table 4.1: Bill of materials for MFC feather construction

Quantity	**Name of Item**
1	Vacuum Pump
2 ft^2	Carbon Fiber
2	M8528-P1 MFCs
2	M8528-F1 MFCs
2 ft	Wire
1	Soldering Iron
7 ft^2	Stretchlon 200
3 ft^2	Nylon Peel Ply
1 roll	KPT2-1 1/2 2 mil Kapton Tape
3 ft^2	10oz Breather
1 roll	Sealant Tape
1	Bag Valve
1 canister	West 105 Resin
1 canister	West 205 Fast Hardener

Figure 4.1: Picture of vacuum bagging process on the MFC test article

The first phase of laying up the article and vacuum bagging involved only the carbon fiber. Two plies of 3k weave were soaked in epoxy and placed at 0°/90° orientations. The size of the carbon fiber was significantly larger than the desired 35 mm × 160 mm area of the feather (Figure 4.2). Note that the finished feather has a nominal thickness of 0.6 mm. This over-sizing of the carbon fiber allowed for optimal placement of the bag valve and later MFCs. The next phase began with cutting one corner of the carbon fiber to a 90° angle to act as one corner of the feather and subsequently, as a datum to align the MFCs. The two inner bending MFCs were epoxied and vacuum-bagged next. Before being lain up, the wires were soldered to the MFCs' electrical leads for ease of connection later. The last phase of the layup involved applying layer of Kapton tape and placing the twisting MFCs directly on top of the bending MFCs (Figure 4.3). The Kapton layer is necessary as an electrical insulator between MFCs.

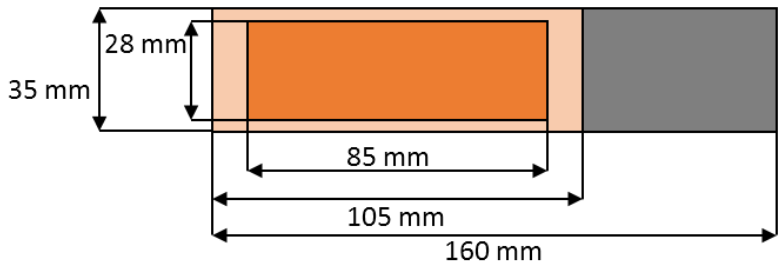

Figure 4.2: MFC Feather Dimensions

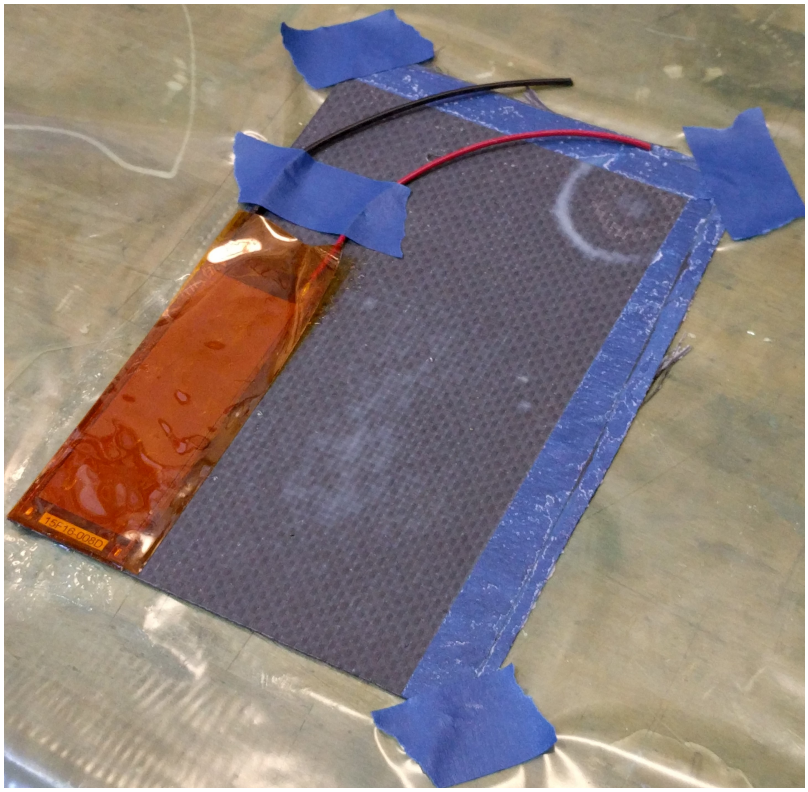

Figure 4.3: Second layup of bending MFCs

The excess carbon fiber at the base of the feather not covered by the MFCs is where the feather was clamped during testing (Figure 4.4). The figure below shows the final test article that underwent both the static and wind tunnel testing.

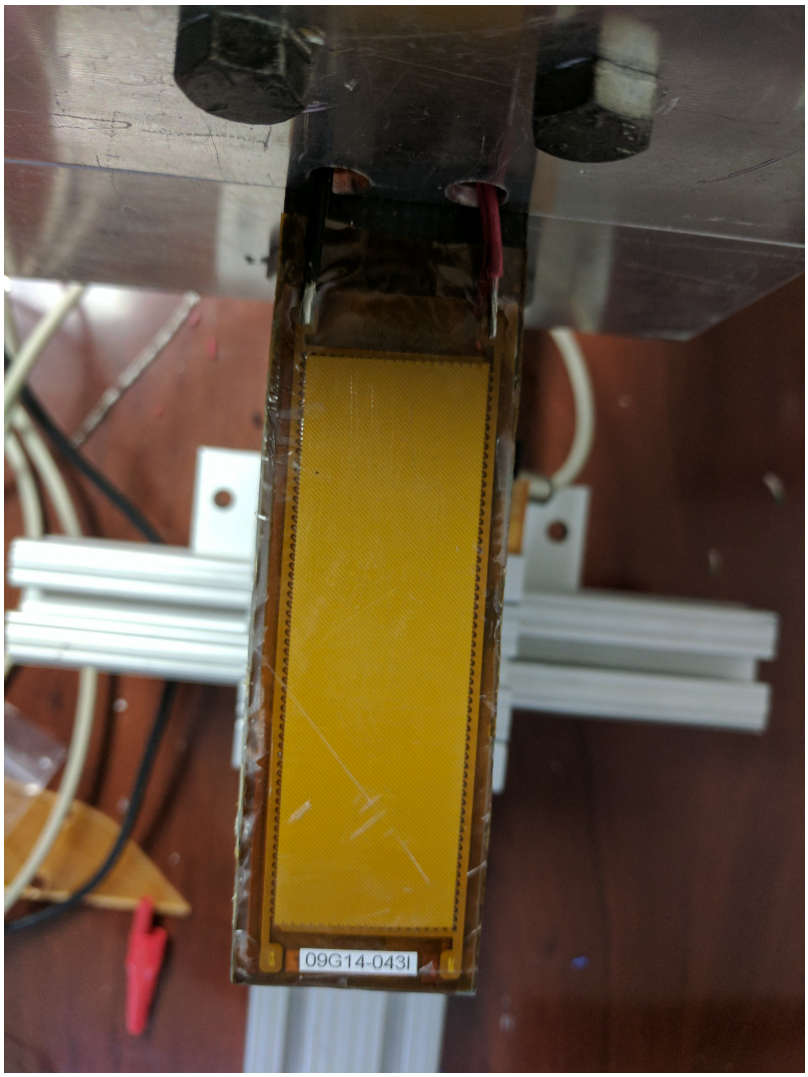

Figure 4.4: MFC feather as a test article

4.2 Experimental Rig and Instrumentation

Measuring static deflection required the use of several different instruments and tools. Note that all equipment was chosen with use in the wind tunnel test in mind. The largest and most important piece of equipment was the experimental rig, which was designed and built specifically for these experiments. The rig (Figure 4.5) was constructed from the extruded aluminum rails. This choice to make the rig out of Series 15 80/20 was made for two reasons: the wind tunnel

frame was constructed out of 80/20, making mounting the rig to the frame easy and it allowed for ease of manufacturing and design with all the desired elements readily available. The rig consists of two cantilevered arms, the top holding the test article and the other, slightly longer, lower arm holding a laser rangefinder. The laser rangefinder is free to move along two axes thanks to two linear bearings. The laser rangefinder was used to make a matrix of points along the feather to characterize the deflection. To measure the placement of the laser rangefinder, two strips of adhesive measuring tape were placed underneath the bearings. This measuring tape allowed for relative locations of the rangefinder to be accurately recorded.

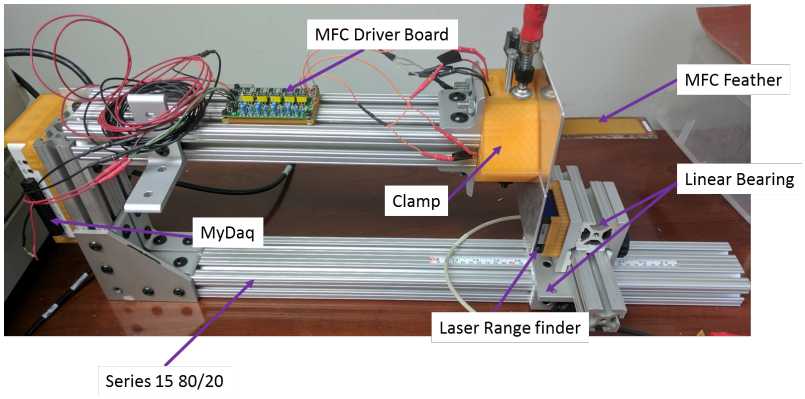

Figure 4.5: Experimental rig

To measure displacement of the MFC, a Micro-Epsilon optoNCDT 1401 laser rangefinder was used (Figure 4.6). This rangefinder has an operating range between 60 mm and 200 mm with a resolution of 40μm, ideal for the range and deflection required by the experiment. The rangefinder had to be placed sufficiently far from the test article that it would not interfere with aerodynamics in the wind tunnel, but still close enough to capture the deflection of the feather. The calibration process for the rangefinder can be found in Appendix B. The laser rangefinder outputs a current proportional to the distance measured. This current was measured by the data acquisition unit and recorded. All technical information used was found in the manual ([21]).

Figure 4.6: Micro-Epsilon optoNCDT 1401 Laser Rangefinder

A National Instruments myDAQ was used for data collection and control of the system. This allowed for control of the MFC via a driver board discussed later. The myDAQ connects to a computer, in this case a laptop, running a LabView code.[22] This code was generated in two parts specifically for this experiment. The first part controlled the actuators and sent voltages to the driver board. The second part collected the data from the laser rangefinder. It averaged the incoming current over five-second intervals and removed any outliers. The measured current was then recorded and post-processed for analysis. The myDAQ connected to the computer via USB and to the laser rangefinder and MFC driver board via analog input and analog output, respectively (see Figure 4.7).

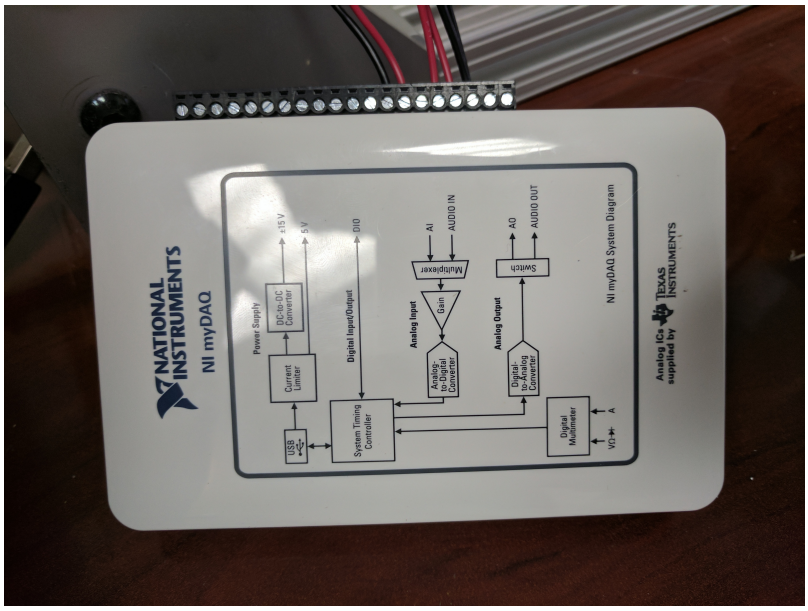

Figure 4.7: National Instruments myDAQ

The next piece of equipment necessary to the experiment was the MFC driver board. The Dual Channel MFC Bimorph High-Voltage Driver by Avid LLC took 0-5 volt signals corresponding to -100% and 100% actuation, respectively, and provided the appropriate voltage to the MFC bimorph. At a signal of 5 volts, one MFC would receive 1500 V (transformed from an outside source) and the other MFC would receive -500 V (Figure 4.8)[10].

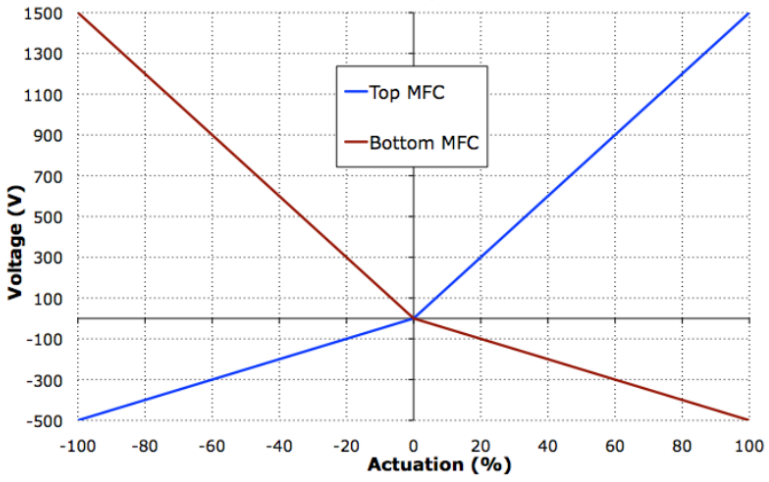

Figure 4.8: Voltages provided to the MFC bimorph by the Avid board ([10])

The board (Figure 4.9) is capable of driving two MFC bimporphs or one feather. However, because the twisting bimorph is not the bimorph originally intended for the driver, both leads of that bimorph are attached to a single output, HV1, rather than HV1 and HV2. This makes both the top and bottom 45° angle MFCs actuate at the same percentage, causing torsion as desired. While not tested, this increased load on one output will cause the MFC bimorph to actuate at a slower rate, as there is now double the capacitance on one channel.

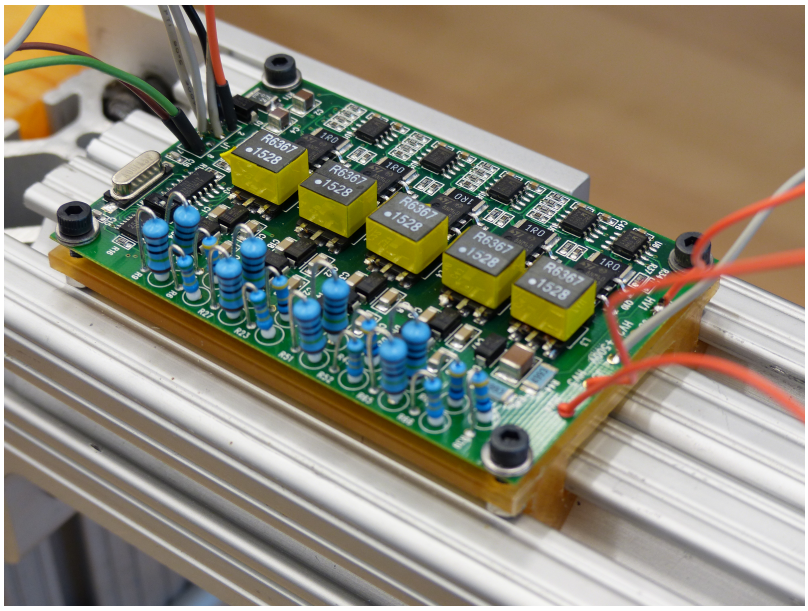

Figure 4.9: AVID-EHV-MFC.B2 MFC bimorph driver

This experiment actuates the MFCs to their maximum positive or negative actuation, -100% or +100%. This avoids the MFCs' inherent hysteresis. Hysteresis, in this case, means that the position of the actuator is not only determined by the input given, but also by the previous positions. While this is not within the scope of the experiments conducted in this research, hysteresis could affect the real-world implementation of the MFC feather. A more graphical explanation (Figure 4.10) from Eric Gustafsons work shows the extent of this problem ([11]).

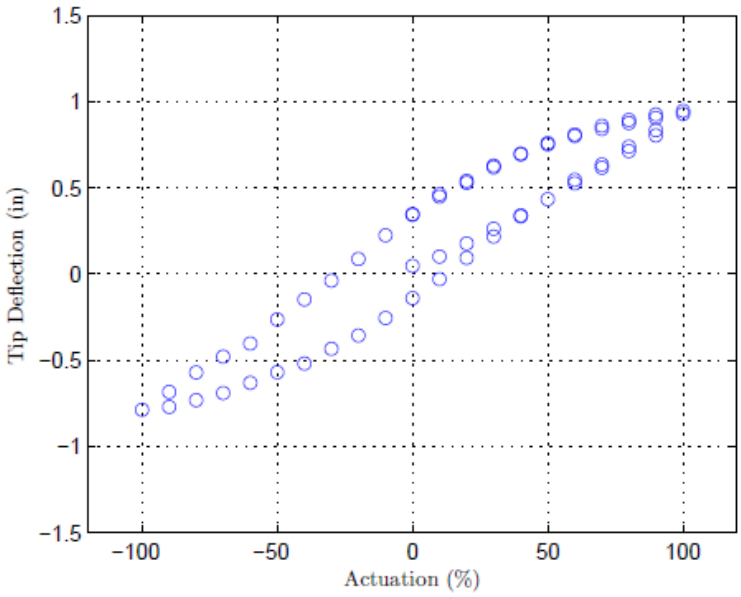

Figure 4.10: The hysteresis effect experienced by MFC actuators sweeping from 0% → 100% → −100% → 100% → 0% ([11])

The laser rangefinder and Avid MFC driver both require a constant voltage to operate. To provide the necessary voltage, two power supplies were used (Figure 4.11). They were set to 12 V for the MFC driver and 20 V for the laser rangefinder as prescribed in their respective manuals ([10],[21]). Note that there was no external power source required for the myDAQ, which ran purely off of USB power.

Figure 4.11: Power supplies used for the MFC driver and laser rangefinder

Once all of the equipment and rig were set up the experiment could commence. The MFC was clamped in place using two orange 3D printed blocks. The MFC was then suspended, cantilevered, over the laser rangefinder. The laser rangefinder was calibrated and then placed into its 3D printed holder. Then the data acquisition could begin. The MFCs were driven to the desired actuation level and the laser rangefinder was moved through a sweep of locations taking data at each point. The locations for each point stayed constant for every test including those in the wind tunnel (Figure 4.12).

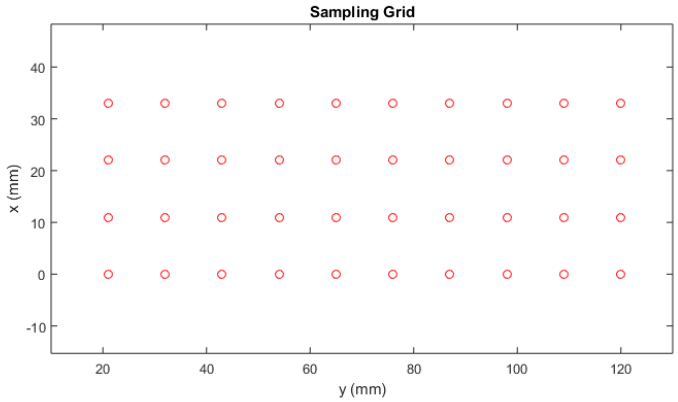

Figure 4.12: X and Y location of each sample point for the MFC feather.

4.3 Wind Tunnel and Instrumentation

The wind tunnel experiment employed the same measuring procedures and apparatus as the static testing, with the addition of the wind tunnel and its requisite instrumentation. 3D printed mounts for the myDAQ and MFC driver board were designed to secure the instrumentation to the rig during testing. A metal end plate was cut for the clamp as an effort to reduce unnecessary turbulent flow caused by the clamp and rig (Figure 4.13).

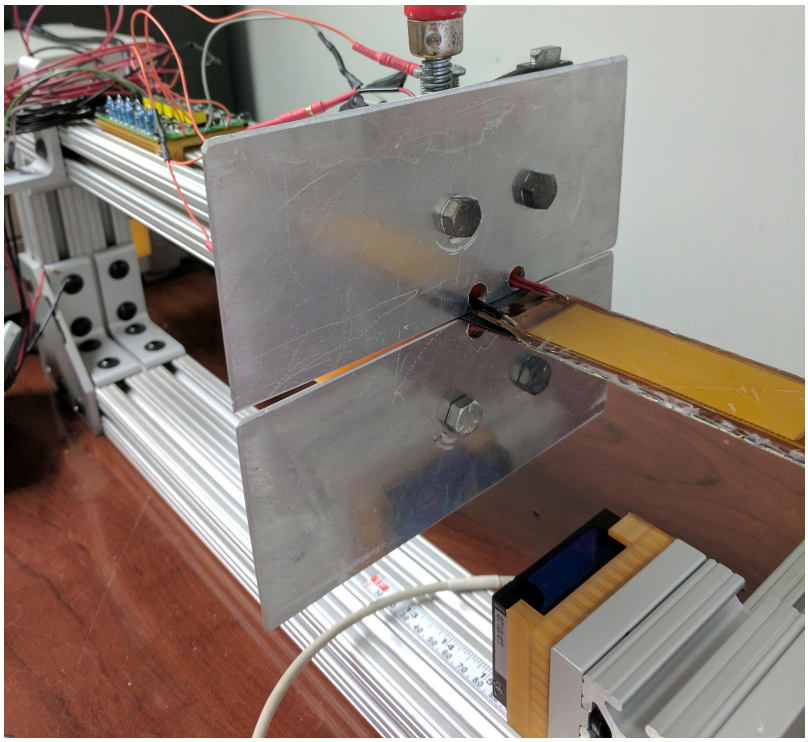

Figure 4.13: Metal end plates for wind tunnel testing

The wind tunnel used was the subsonic open-jet wind tunnel at Virginia Tech (Figure 4.14). The fan, driving the wind tunnel, produces, with substantial turbulence, a flow of 15 m^3/s. To convert this flow to a uniform, low-turbulence flow, air is directed first through a settling chamber and then through a honeycomb structure and three turbulence reduction screens. Following these stages the flow is accelerated through a contraction nozzle of a 5.5:1 area ratio. The open-jet's motor is capable of running at a maximum fan speed of 1180 RPM, which translates to a maximum flow velocity of 30 m/s. To control the velocity of the flow, the motor speed must be changed; there is no direct control for velocity. The velocity can be measured using the temperature and a dynamic pressure probe.

Figure 4.14: 0.7 meter subsonic open-jet wind tunnel

The experimental rig used in the static testing was also used in the wind tunnel. The rig was attached to the wind tunnel test section frame using two L-brackets (Figure 4.15). The rig places the feather near the center of the 0.7 m width of the wind tunnel. This allows the feather to experience minimal turbulence. The steady flow deteriorates close to the edges of the nozzle exit and this turbulence propagates out as the flow travels downstream. The test article was thus placed as close to the center of the nozzle exit as possible.

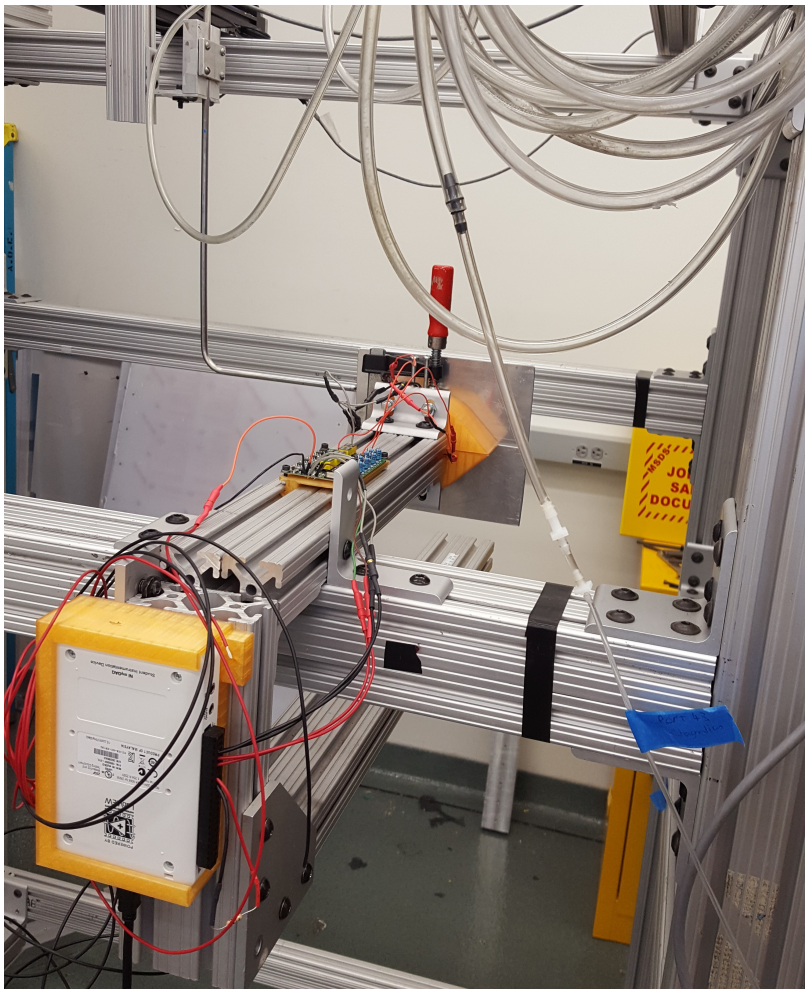

Figure 4.15: Experimental rig mounted to the wind tunnel test section

Deflection data were collected using the same instrumentation used in the static testing. Freestream flow data were collected using a few other instruments including: a barometer, thermometer, NetScanner, and extra laptop (Figures 4.17, 4.16, and 4.18). To read the wind tunnel data, a computer running a Matlab script was interfaced with the NetScanner. For each trial, the only data taken from the computer was the freestream velocity. The calculation for the velocity required the temperature and pressure to be entered first into the computer. The net scanner (see Figure 4.16) reads the pressure ports from the instruments and relays them to the computer. To calculate the velocity, the ambient temperature and pressure must be entered manually. They were measured using the barometer (Figure 4.17).

Figure 4.16: The NetScanner used to read pressure ports in the wind tunnel

Figure 4.17: the barometer and thermometer used to measure ambient conditions

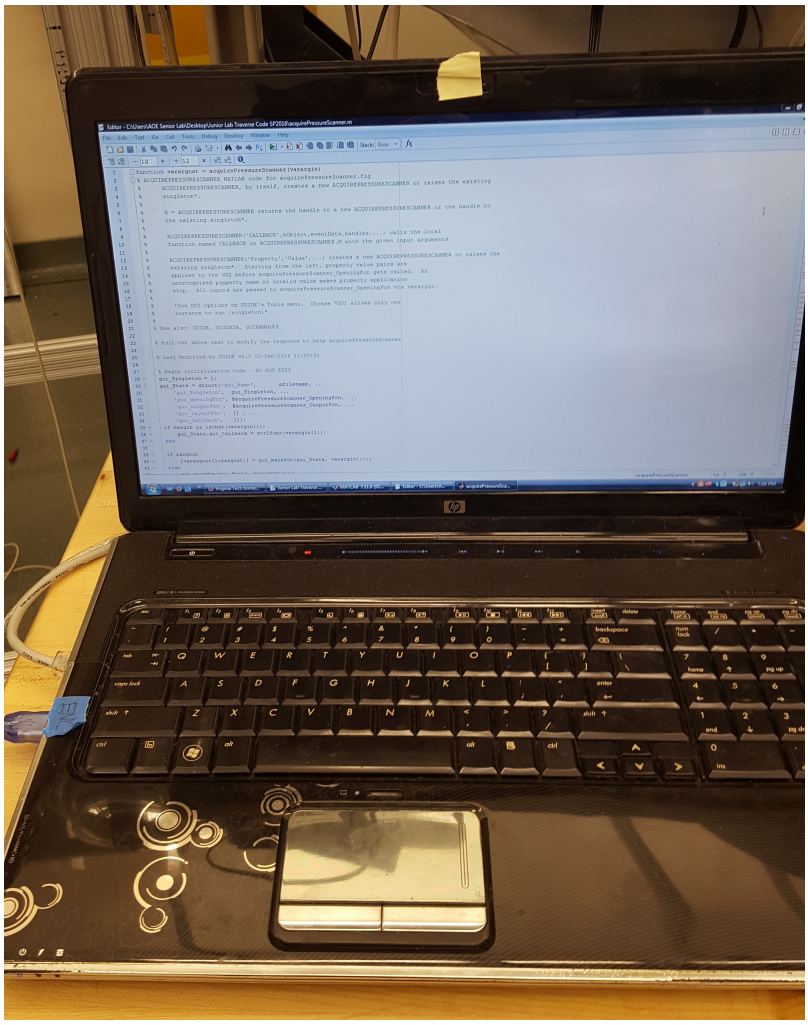

Figure 4.18: Wind tunnel computer that reads in the net scanner

The Matlab code run by the wind tunnel laptop calculates the freestream velocity using equations 4.1. See Appenix A for a sample calculation and the uncertainty for each trial. In this equation, p_0 denotes the total pressure (that is, the room's ambient pressure), p is the static pressure in the flow, ρ is density of the flow, and U is the flow velocity.

$$U = \sqrt{\frac{2 * (p_0 - p)}{\rho}} \tag{4.1}$$

Air density was calculated using the perfect gas law (equation 4.2) where R is the gas constant $287\frac{\mathrm{J}}{\mathrm{kg\,K}}$ and T is temperature. [23]

$$p = \rho RT \tag{4.2}$$

Next the Reynolds number was calculated using equations 4.3, 4.4, and 4.5. In these equations, μ is the dynamic viscosity, ν is the kinematic viscosity, Re is the Reynolds number, T is the temperature, U_∞ is the freestream velocity, and c is the defining length characteristic of the object in the flow (typically chord length).In this case c is the chord length of the feather, 35 mm ([23]).

$$\mu = \frac{1.4578 \times 10^{-6} T^{1.5}}{T + 110.4} \tag{4.3}$$

$$\nu = \frac{\mu}{\rho} \tag{4.4}$$

$$Re = \frac{U_\infty c}{\nu} \tag{4.5}$$

For each trial, the Reynolds number and freestream velocity were calculated once the wind tunnel had reached a steady state. The steady state desired for this experiment may be defined as, the time where the wind tunnel fan is no longer accelerating its fan and the MFC feather has found an equilibrium deflection within the flow. After these quantities were computed, the recording of the MFC feather's deflections could commence. The same points for the sweep were used as described for the static test (Figure 4.12). The displacements of the MFC were recorded for both the undeflected shape in the flow and the deflected shape, bending down and twisted "up", in the flow. The twist up convention was taken from the static test, but the twisting down

of the MFC is actually a decrease in angle of attack. This actuation scheme allows for the largest deflections at a given flow.

Chapter 5

Experimental Results and Discussion

This chapter first describes the results of the static and wind tunnel testing. Afterward, these results will be discussed in terms of both physicall significance and possible sources of error.

5.1 Static Testing

The first tests run on the MFC feather provided a base measurement of the static, undeflected shape. The surface plot of these measurements (Figure 5.1) shows a rough, uneven surface. This unevenness stems from inconsistencies in production and inherent geometry of the feather. The feather itself has ridges on its surface where the active area of the MFC patch ends. The feather also has unavoidable raised sections close to the soldered leads. Finally, some of the roughness may be attributed to pooling on the surface. When laying up the feather not all epoxy was sucked out of the model; this lead to pooling of epoxy and unevenness on the feather's surface. Another error, unrelated to the MFC feather itself, came from the experimental rig. By introducing the rig to the open jet flow causes a blockage. This blockage causes changes in the flow, including dynamic pressure and angle of attack. While there was no way of determining the angle of attack change caused by the experimental rig, the change in dynamic pressure was accounted for by measuring the dynamic pressure using a pitot tube near the test feather.

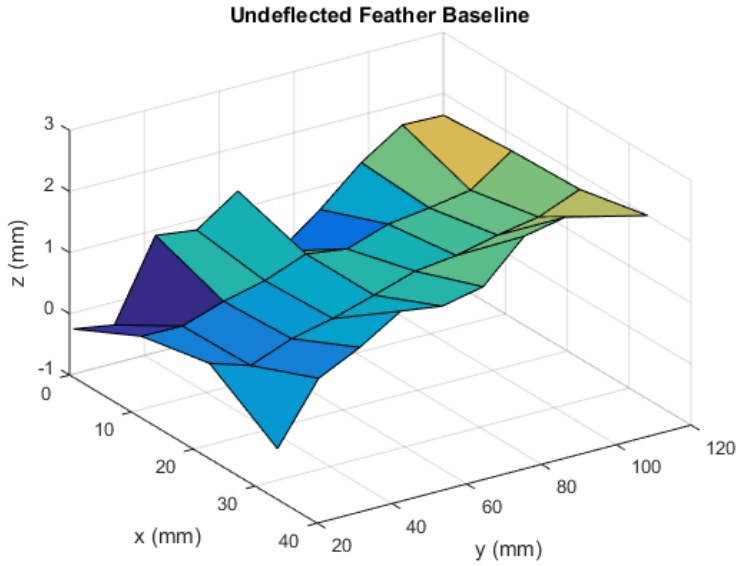

Figure 5.1: Characterization of the undeflected MFC feather

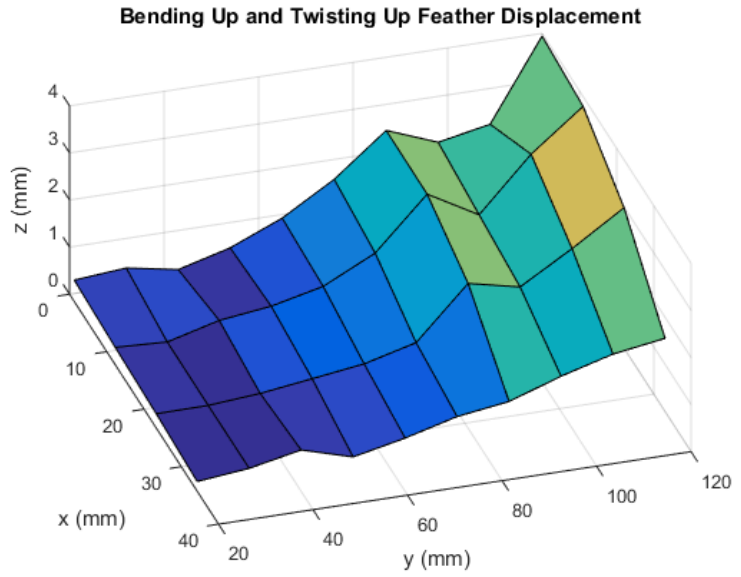

Figure 5.2: Deflection of MFC Feather while both bending up and twisting up

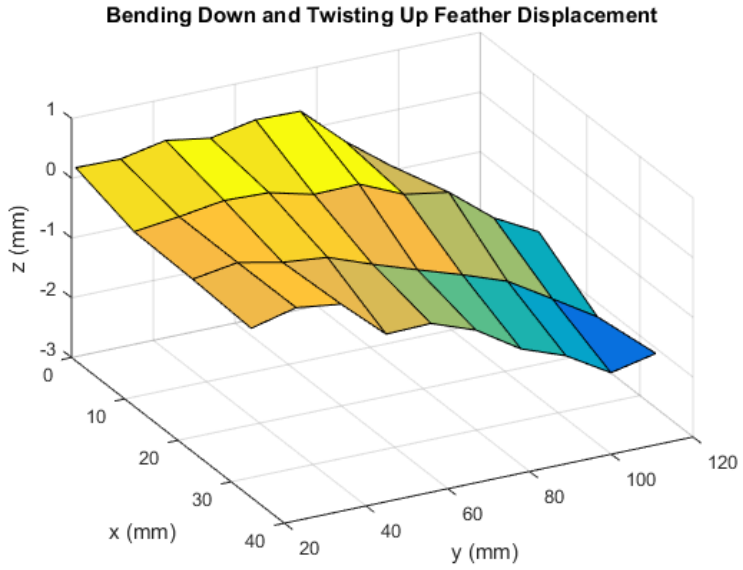

Figure 5.3: Deflection of MFC Feather while both bending down and twisting up

From Figures 5.2 and 5.3, it is clear that the data collected on the sides of the MFC feather are not the most accurate. These inaccuracies could have been caused by the aerodynamic testing itself. There was immeasurable turbulence caused by the experimental rig which could cause inconsistent deflections of the feather. To measure the tip deflection, the twist and bending was derived from the center two points. When comparing the combined deflections measured to that of the FEA model, small but acceptable error is found (Table 5.1). The error in deflection magnitude was under fifteen percent, an adequate margin. Equation 5.1 was used to solve for the twist angle. δz is the deflection at point i, j, where i denotes the x location index and j denotes the y location index. The locations in the center of the feather, $i = 2,3$, were used as the outer edge locations did not provide reliable data.

$$\phi = \arctan \frac{\delta z_i j - \delta z_i j}{11} \tag{5.1}$$

Table 5.1: Comparison between static test and FEA results

Deflection Mode	FEA Value	Experimental Value	Difference	Percent Error
Bending (mm)	3.9535	3.3875	-0.56599	-14.31
Twisting (rad)	0.07995	0.073425577	-0.006525	-8.161

Several sources of error contributed to the discrepancies in these results. First, the manufacturing procedure introduced some unavoidable defects into the feather. Because the entire feather including the host material, were laid up by hand, there were many opportunities for defects to form. For instance, the carbon fiber was not a constant thickness and some regions received more epoxy than others, causing differences in stiffness. Another flaw in the feather was the placement of the MFCs themselves, which slid slightly during layup. This meant that the MFCs operated slightly off of the desired angle. Lastly, the Kapton tape placed between the MFCs for insulation was left out of the FEA model. These inconsistencies in the feather caused the test article to be stiffer and thus experience smaller actuation magnitudes than those originally predicted.

The next step in the analysis was to characterize the actuation deformation along the span of the test feather. First, the bending deformation seems to be accurately described by a quadratic curve (Figure 5.4). The center-line was calculated by averaging the deflections of the middle two values at each y location. The bending deflection plot shows a high correlation to the quadratic fit and had a calculated R^2 value of 0.9578. This relationship was exploited later in Chapter 6 to build the aerodynamic model.

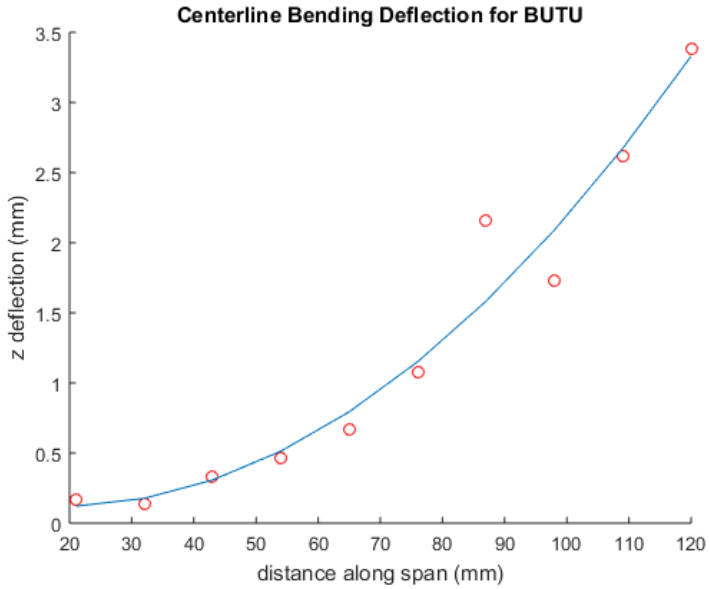

Figure 5.4: Z deflection of the feathers center-line as a function of span

The second deformation mode, twisting, followed the expected path of deflection versus span relationship (Figure 5.5). The feather exhibited a linear increase in twist along the span. This confirms the expected relationship shown previously in the rotor twisting ([1]). The coefficient of determination for this fit was found to be 0.9432. This value does not account for the anomalous eighth point at the y location of 98 mm, which was excluded.

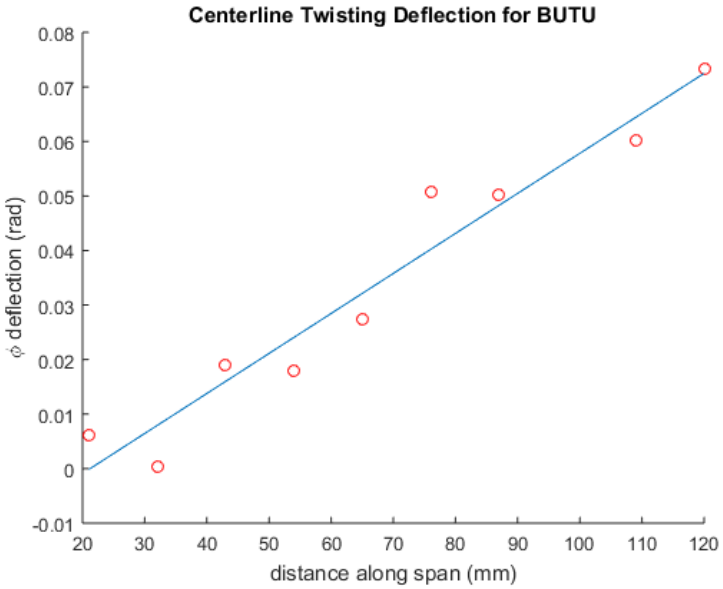

Figure 5.5: Rotational deflection of the feather as a function of span

These results indicated that translating feather geometry into an aerodynamic model will be straight forward. Twist will vary linearly along the feather and the quadratic curves of bending can be modeled with discrete linear panels. The results also show that the deflection of the feather can be accurately estimated by finite element analysis techniques.

5.2 Wind Tunnel Testing

The wind tunnel experiment was devised to characterize the performance of the MFC feather under aerodynamic loading. Specifically, the experiment was designed to calculate the maximum displacements the feather could reasonably achieve in steady, level flight. The experiment was designed to ensure that the feather would not undergo aeroelastic divergence or flutter. The same grid of sampling points were collected as in the static test. However, the final displacements were measured against the undeflected shape at the given freestream velocity. While, some enlightening results mmight arise from a comparison of the total deflection with the static undeflected shape, this experiment offers no way of verifying the static feathers angle of attack.

Any lift and moment generated by the feather while undeflected would alter the results in ways that would be impossible to measure. The wind tunnel test was conducted at freestream velocities of 10 m/s to 25 m/s in 5 m/s intervals. The deflections have been plotted in Figures 5.6–5.9.

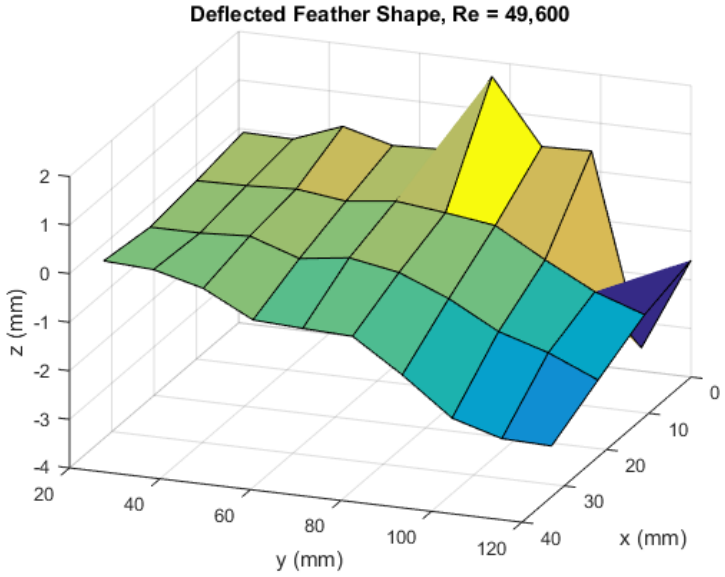

Figure 5.6: MFC feather deflections at a freestream velocity of approx 10 m/s

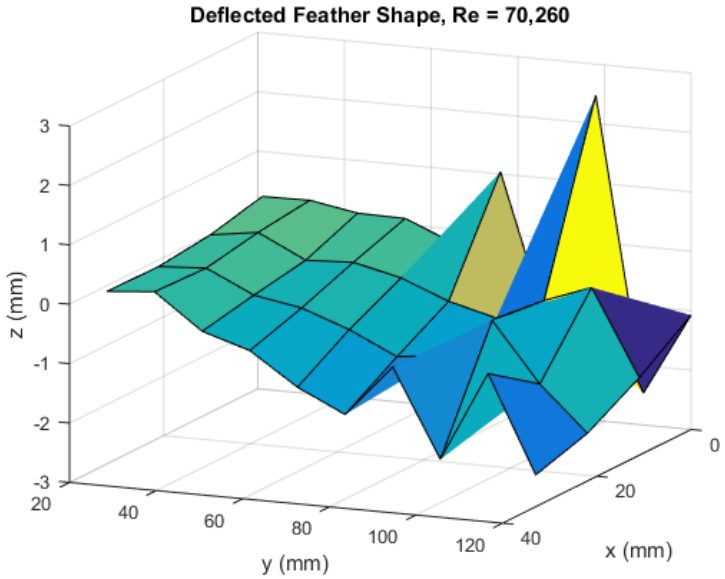

Figure 5.7: MFC feather deflections at a freestream velocity of approx 15 m/s

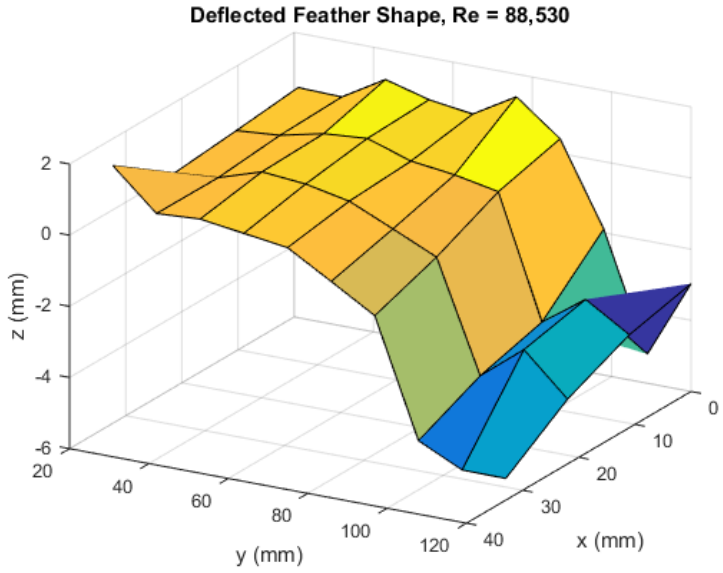

Figure 5.8: MFC feather deflections at a freestream velocity of approx 20 m/s

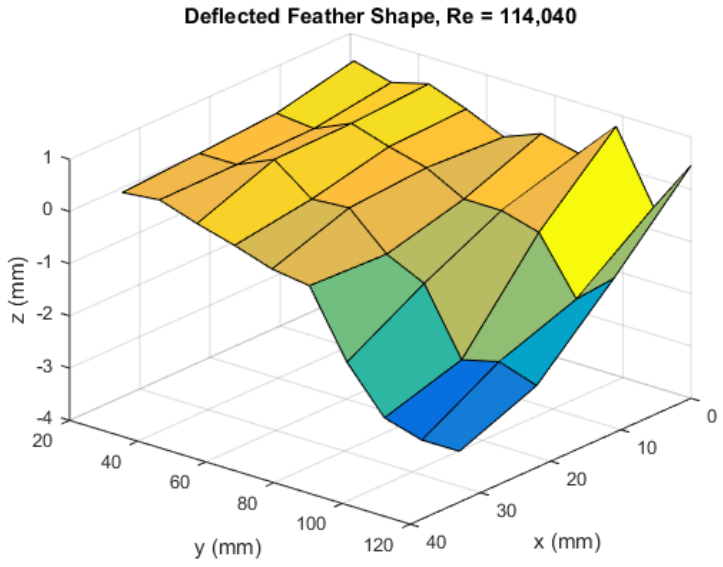

Figure 5.9: MFC feather deflections at a freestream velocity of approx 25 m/s

These plots of the reconstructed surface show some of the same characteristics as the previous static experiment. The middle measurements show much more consistency than the displacements along the edges. This was most likely due to defects in the test article or the laser

measurement system, as described in Section 5.1. The same approach was taken to determine tip deflection in each case, where the two middle points at (11,120) and (22,120) were averaged and evaluated using equation 5.1. These deflections are plotted against the Reynolds numbers in Figures 5.10 and 5.11. The deflections taken in this wind tunnel testing had larger margin for error than those taken the static testing due to small vibrations in the test rig caused by the tunnel. Because the rig was cantilevered, even small perturbations could easily throw off the laser rangefinder's readings. During the tests the MFC feather did not experience any of the failure modes originally predicted. Even at the maximum 25 m/s velocity, the feather experienced no flutter or aeroelastic divergence. This could indicate that the feather was constructed with too much stiffness and that there is a margin for performance enhancement, given a less rigid member. However, to determine the effectiveness of a more flexible feather, more tests would need to be performed and more loading cases would need to be considered.

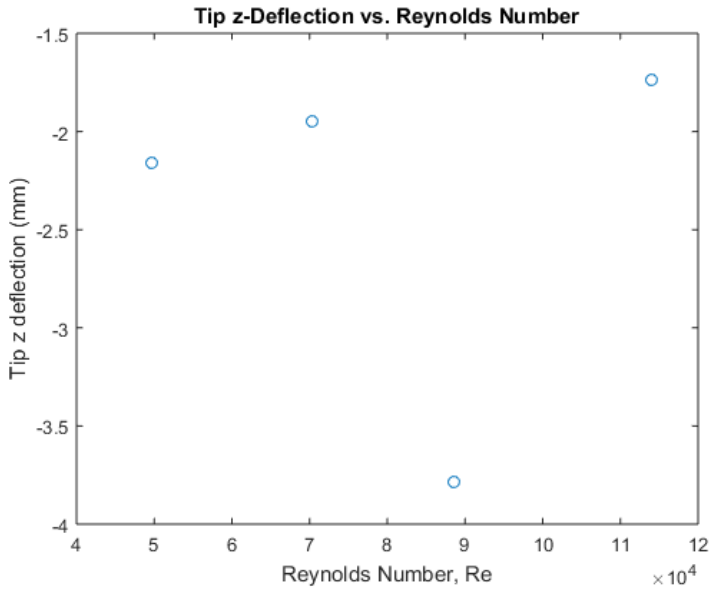

Figure 5.10: Bending z deflection at tip versus Reynolds number

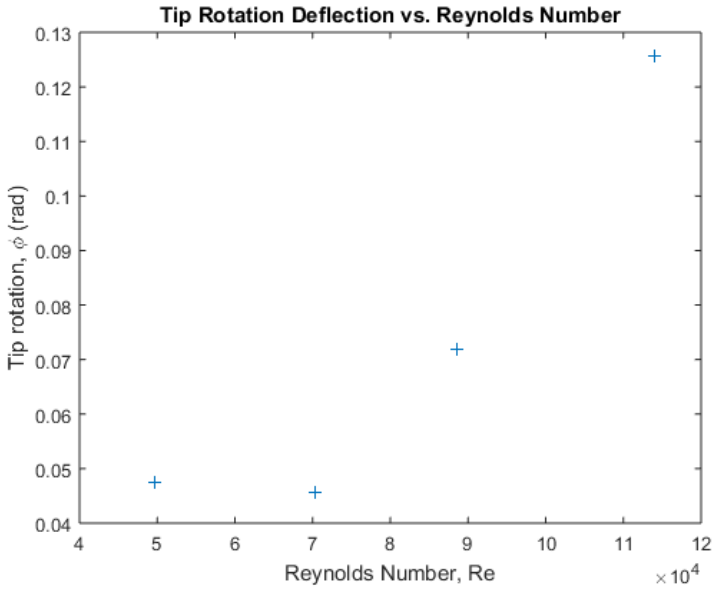

Figure 5.11: Twisting deflection at tip versus Reynolds number

While the static testing yielded results closely resembling the predicted deflection, the wind tunnel testing data did not resemeble the predicted trend as closely. From the Figures 5.10 and 5.11, it is clear that the results from the wind tunnel testing show no clear trend. Originally, it had been predicted that the twisting and bending deflections would increase quadratically with freestream velocity. This is partially because not enough data points were collected. While more freestream velocities would have been advantageous, the open jet wind tunnel did not produce a steady enough flow facilitate testing at a finer interval. Because the temperature and pressure in the room varied over time, the velocity varied over the course of the experiment also because the sampling grid takes so long, a finer testing interval would be impossible. Moreover, the feather had no way to account for hysteresis, meaning that the undeflected shape for each test case was slightly different. However, these deficiencies in the experiment do not detract from the value of the information obtained. The experiment demonstrated that the MFC feather did not experience any failure modes at the assumed freestream velocities while at full deflection.

5.2.1 Wind Tunnel Testing Procedure Improvements

A number of improvements on this experiment could be made to produce better results. First, for both the static and wind tunnel experiments the use of a laser profile scanner would eliminate the need to measure a sample grid, a process which proved to be both inefficient and inaccurate. An example of such a profile scanner is sold by the same company which manufactured the laser rangefinder, Micro-Epsilon. The scanControl series 2600-100 would work well in this role ([24]). By using this measurement technique, the wind tunnel testing would be allowed to run at finer intervals for freestream speed. Another improvement on the wind tunnel experiment would be to use a more aerodynamic rig such that wall effects on the MFC feather would be minimized. Lastly, the wind tunnel testing would be more accurate if the experimental aparatus included a hysteresis measurement device and a means of "zeroing" the feather's angle of attack.

Chapter 6

Aerodynamic Model

The next step in analysis of the feather is to test its aerodynamic properties. Because the feather demonstrated stability in the wind tunnel testing, research could commence to determine whether or not the feather could provide the aerodynamic benefits seen in birds to fixed wing aircraft. The aerodynamic analysis was performed using the Tornado, as discussed in the literature review. This was also the program in which the wing model was built.

The dimensions of the test article were used to determine the size of the wing. First, the number of tip feathers was chosen to be four per side. Any less than four feathers would not accurately model a smooth camber line or the +8 tip feathers seen in birds ([25]). Any more feathers would make the wing's aspect ratio too small to produce an efficient enough wing. Given four feathers, each 10.5 cm in length, the wingspan was set at 1.4 m. This span would give the feathers about 15% span, close to the 14% described in [5]. For spacing between feathers the nominal distance of 0.5 cm was chosen, yielding an acceptable aspect ratio of 6.25. The profile of this wing can be seen in Figure 6.1. The feathers have inboard twist equal to that of the camber of the airfoil to which they are connected. The main wing is comprised of two sections. The inboard section is a NACA 2412 airfoil 0.295m in length which twists from 5° inboard to 1° outboard. The outboard section is 0.3m long and transitions from a NACA 2412 to the thinner, camberless NACA 0008 to ease into the feathers. This section twists from 1° inboard to −3° outboard. The feathers on

each side start with an inboard twist of −3°. They twist linearly downward as they go outboard to one half their twisting range at the tip, 0.055 radians or 3.2 degrees, so the outboard tip of the wing is at a twist of −6.2°. The feathers transition from a dihedral angle on the leading feather to anhedral angle on the aft feather, similar to the tip feathers of many birds of prey.

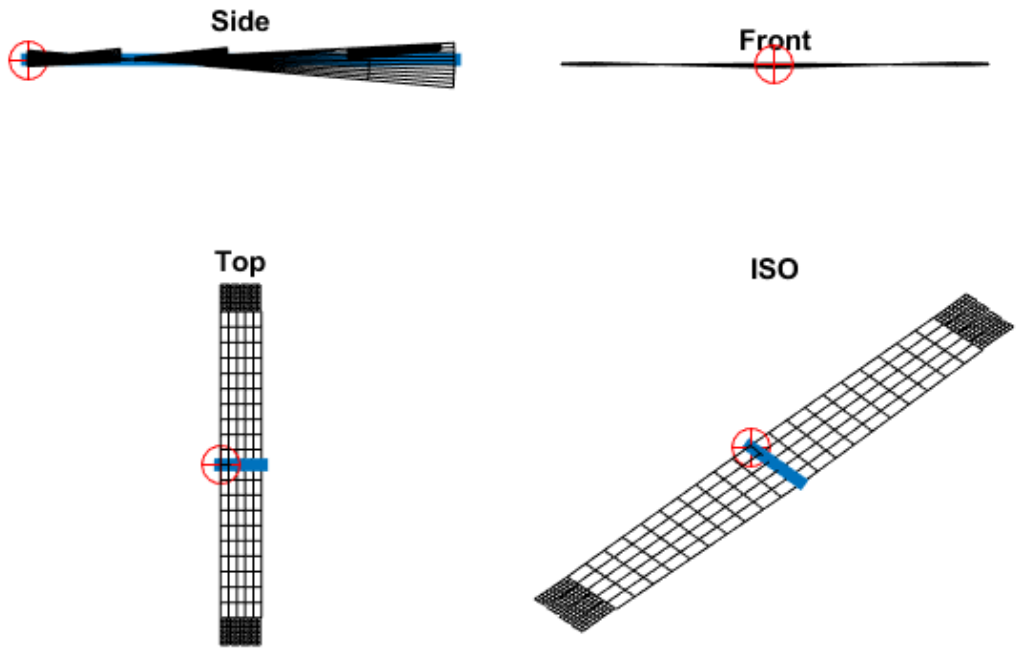

Figure 6.1: All views of the feathered wing model

For the steady level flight analysis, the cruise conditions were set as an angle of attack of 0° and a freestream velocity of 20 m/s. All other parameters, like sideslip angle and roll rate, were set to zero with standard sea level atmospheric conditions. The results of the aerodynamic analysis of the feathered wing were compared to those of a rectangular wing of span equal to 1.1667 m. This gave a span ratio of 1.2:1 between the feathered and standard wings. The standard wing was implemented two sections like the feathered wing, one inboard with a span of 0.2833 m and one outboard of span 0.3 m. The inboard section had a NACA 2412 airfoil and went from an incidence angle of 2.1° inboard to 2° outboard. The outer section of the wing went from 2° angle

of attack inboard to 3° outboard (Figure 6.2). While this did not give a perfectly elliptical wing loading it is close enough to compare. Ailerons had been added to the outboard section of the rectangular wing to induce a rolling moment in later tests.

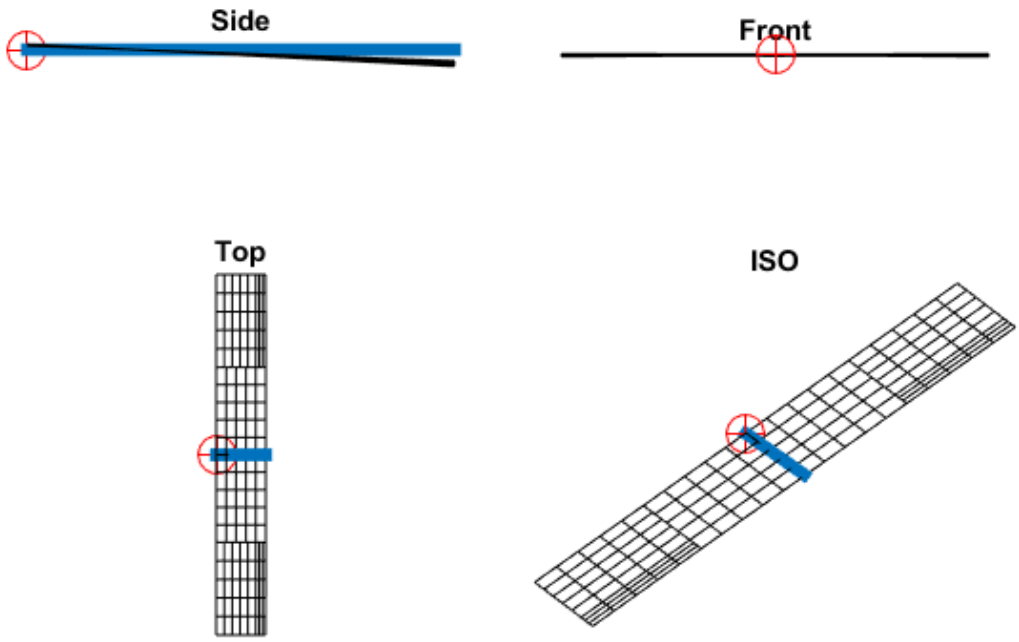

Figure 6.2: All views of the standard wing model

These two aerodynamic models were tested in two cases to asses the ability of the MFC feathers at to induce proverse yaw and decrease induced drag. In the first test, both the wings were placed under steady level cruise conditions to measure baseline drag. The angle of attack of each wing was then varied to find the zero lift angle. At this angle, the drag was measured again. Using equation 6.1, the induced drag in each cruise case may be computed. In this equation, C_d is the drag coefficient, C_{d0} is the drag at zero lift, and C_{di} is the induced drag ([26]).

$$C_d = C_{d0} + C_{di} \tag{6.1}$$

The second of the two tests determined proverse yaw effects. Both wings' control surfaces were deflected asymmetrically in steady level flow. Then the roll and yaw moments were computed and compared. If these two tests demonstrated a reduction in induced drag and opposite signs for yaw moments, then the feathered wing would have proven it could increase structural efficiency and induce proverse yaw.

Chapter 7

Aerodynamic Model Results

This chapter presents the aerodynamic results from analyses performed on the Tornado models developed in Chapter 6. This section presents data demonstrating the feathers' effectiveness in reducing induced drag and inducing proverse yaw.

7.1 Induced Drag

The first step in computing induced drag of the standard and feathered wings was to run Tornado analysis of each at the steady state conditions. This yielded unexpected results in the lift distribution curve of each wing (Figures 7.1 and 7.2). While both produce the same amount of lift it is evident that vastly different distributions produced. The standard wing achieves a nearly almost elliptical lift distribution, as desired. The feathered wing, on the other hand, produces a bell-shaped lift curve like those discussed by [5].

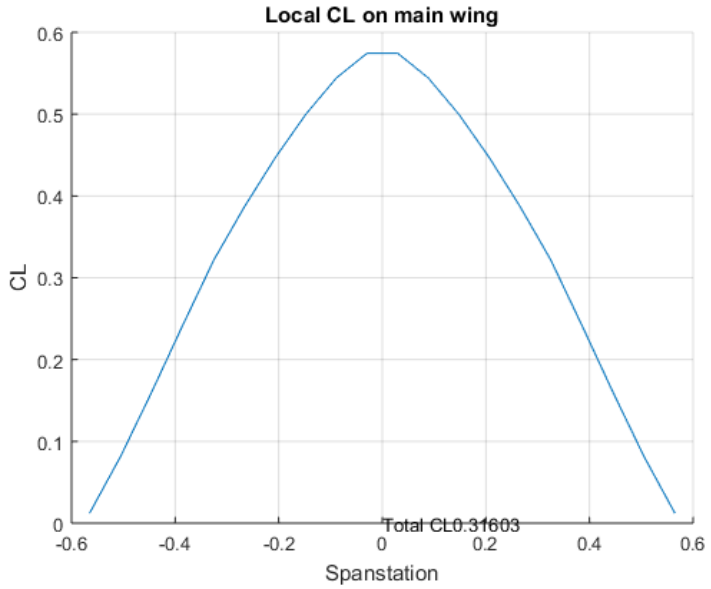

Figure 7.1: Spanwise lift distribution along the feathered wing not including the feathers

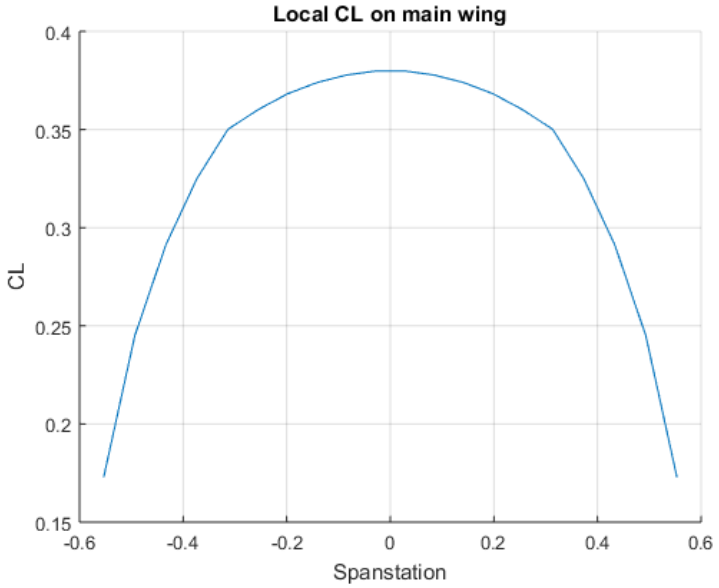

Figure 7.2: Spanwise lift distribution along the standard wing

The next step in the aerodynamic analysis was to determine the zero-lift drag. Both wings were analyzed at different angles of attack to estimate α_0. The zero-lift angle of attack, α_0, for the

feathered wing and standard wing were found to be −3.136° and −4.017°, respectively. Results from both the zero-lift and steady level flight runs are presented in Table 7.1.

Table 7.1: Tabulated results for the steady level and zero-lift flights

	Feather	**Standard**
Steady Level		
Lift (N)	14.742	14.7737
Drag (N)	0.30942	0.1994
C_{L_α}	5.6305	4.5988
C_{D_α}	0.081501	0.12492
Zero Lift		
Lift (N)	−0.001078	−0.0012498
α (deg)	−3.136°	−4.017°
D_0	0.25576	0.0013042
D_i	0.05366	0.1980958

The results from the zero lift and steady level testing show a significant decrease in induced drag for the feathered wing. The bell shaped lift distribution while producing more drag overall, produces less drag from lift. The traditional elliptic lift distribution generated 0.1981 N of drag while the feathered wing produced 0.05366 N, a 73% decrease. This proves that the feathered wing design implementing the bell shaped lift distribution does in fact reduce induced drag. When comparing the bending moments along the span of the wing, it is evident that the feathered wing has a significant advantage. Because the feathers are not actually connected to the wing, the positive bending moment caused by them is therefore not included (see Figures 7.3 and 7.4). This would have further decreased the magnitude of the bending moment experienced by the wing. While total drag increases due to the feathers, the structural advantages from the feathered design could outweigh this potential drawback.

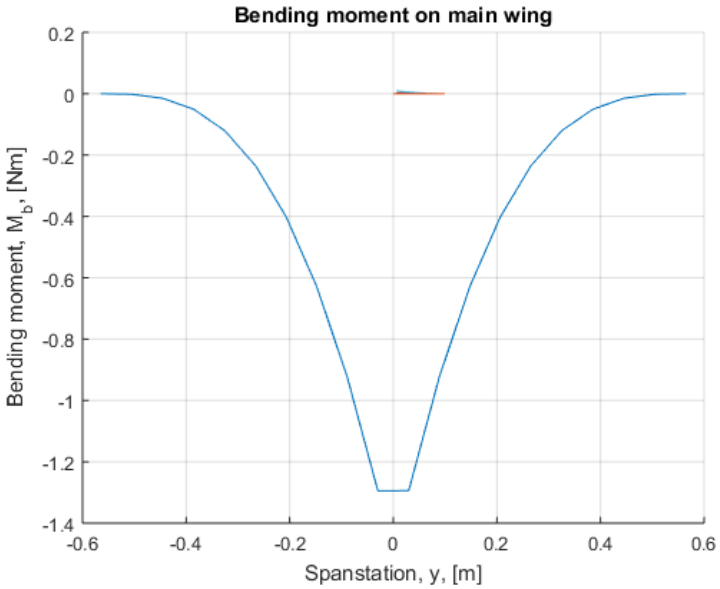

Figure 7.3: Bending moment as a function of span along the main wing of the feathered design.

Figure 7.4: Bending moment as a function of span along the standard wing

7.2 Proverse Yaw

The final step in the analysis of the MFC feather was to determine whether it can induce proverse yaw. Given that the spanwise lift distribution matches that given by Bowers in [5], proverse yaw is likely. To test this hypothesis, the feathers from the model were twisted to their full range approximately 3.2° asymmetrically. That is to say that one half-span the feathers were twisted to +100% and on the other half-span the feathers were twisted to -100%. The results on this wing were then compared to results on the standard wing where the ailerons were deflected asymmetrically by 3°. The results are presented in Table 7.2. The variable, C_{l_δ}, is the change in rolling moment coefficient per degree of control surface deflection.

Table 7.2: Tabulated moments from rolling flight of both feathered and standard wings

Body Moments	**Feathered**	**Standard**
Roll (Nm)	−0.28075	−0.95874
Pitch (Nm)	−0.89245	−0.86772
Yaw (Nm)	−0.01778	0.040272
C_{l_δ}	0.006	0.0017

While the standard wing exhibits the adverse yaw expected with an elliptical lift distribution, the feathered wing shows the opposite. The standard wing's roll moment and yaw moment have opposite signs the definition of adverse yaw. This indicates that the aircraft would be rolling right but yawing left. The feathered wing, however, exhibits proverse yaw: both the rolling and yawing moments have the same sign, signaling that the wing is both yawing and rolling to the right. While these results do show some promise when it comes to inducing proverse yaw, several causes for concern persist. The MFC feather shows significantly lower control authority, signified by the rolling moment induced by the feathered wing being less than a third of that produced by the standard wing. While corrective wing design may be able to alleviate this problem, these feathers likely could not be used for roll control by themselves. If the MFCs could be made more

flexible with a doubled or tripled twisting range, they may have some potential as the sole control system for roll authority.

In conclusion the MFC feathers have proven capable of producing the a bell-shaped lift distribution associated with proverse yaw. In turn this design has significantly decreased the bending moments on the wing and thus relaxed the structural requirements of the supporting members. Finally, while the feathers, when actuated asymmetrically, produce proverse yaw unlike a traditional wing they do not elicit large enough rolling moments to be used as the sole roll-controlling surfaces. Further research into the feathers and wing design implementing them would need to take place before they could be deployed on a real-world aircraft.

Chapter 8

Conclusion

8.1 Summary

This research has explored the use of macro fiber composites (MFCs) to create actuated tip feathers for increased efficiency and control of small unmanned aircraft. MFCs were applied as two bimorphs to a thin carbon fiber layup. This actuator was able to morph in two modes: bending and twisting. When applied to the tip of a wing, this feather offer similar control characteristics to those of birds. The MFC feather was laid up using carbon fiber as the host material because advantageous Poisson's ratio allowing for more strain energy to be dissipated through torsion rather than extension. The feather layup took advantage of the MFC property of inducing strain on the host material to maximize tip deflections. The feather consisted of a carbon fiber layer sandwiched between two MFC bimorphs. The inner bimorph controls bending while the outer controls twisting. The bending MFC bimorph induces strain, top and bottom, in an anti parallel fashion along the feathers longitudinal axis. The twisting bimorph's MFCs act perpendicularly to one another and both at a 45° angle to the longitudinal axis. The bimorphs can be driven independently by a driver board, allowing any combination of deflections within a certain range.

Because any number of deflections could be achieved, this research only focused on the maximum deflections. The feather was analyzed using NASTRAN and a pre-/post-processor called Femap. These models yielded accurate predictions for the real test article's performance. The bending deflections came within 14.31% of predicted values while the the twisting deflections came within 8.161%. These results were compared only to static deflections, as NASTRAN was not used to produce aeroelastic models. The feather was also tested under aerodynamic load in an open-jet wind tunnel. The feather was tested at four freestream velocities between 10 and 25 m/s at 5 m/s intervals. This experiment did not produce many meaningful analytic results, but it did yield several important qualitative insights. During wind tunnel testing, the MFC feather exhibited no aeroelastic divergence or flutter, meaning that it shows great promise for future implementation on an actual aircraft.

Finally, the feather was modeled on an actual wing using the vortex lattice method in Tornado, a Matlab script. This model was compared in induced drag and proverse yaw to a standard rectangular wing. The standard wing had a traditional elliptic lift distribution along the span, whereas the feathered wing was designed to have a bell shaped lift distribution. This lift distribution was chosen to decrease induced drag and generate proverse yaw. Numerical results show that the feathered wing decreased induced drag by about 73% compared to the standard wing. This actuator also shows great promise in structural optimization because it also causes a decreased bending moment along the entire span. Lastly, the feathered wing produced proverse yaw, as opposed to the adverse yaw from the standard wing. While the feathers showed great promise in certain roles, they were not able to produce the same amount of roll moment as traditional ailerons. MFC feathers are far from use on real-world aircraft, but with more research to increase roll authority, they may one day help to make a more efficient SUAS.

8.2 Future Work

8.2.1 Single Crystal MFC and Host Material Thickness

One area for significant improvement is the actuation range of the feather. The small tip deflections of roughly -3 mm to 3 mm and $-1.5°$ to $4°$ leave much to be desired. While these deflections are adequate and can be used effectively to decrease induced drag, large deflections would be beneficial for roll authority and would even further decrease induced drag for higher cambered airfoils.

Deflection magnitude of the feather is tied to the feathers overall stiffness. To decrease the stiffness of the feather, one might consider, decreasing the thickness of the host material and/or decreasing the stiffness of the MFCs themselves. Decreasing the stiffness of the host material (carbon fiber) by using one layer instead of two would decrease the overall stiffness of the feather and thus increase the tip deflections. The other option would be to try single crystal MFCs as described by Park in [1]. These MFC patches while slightly heavier have a much lower Young's modulus and in turn can generate over two times as much the strain as the ones used in this experiment.

While both of these options could generate a more flexible feather, there are several drawbacks to keep in mind. While the new feather would certainly have much larger deflections, it may now be susceptible to flutter and aeroelastic divergence at high speeds. To counteract this, experiments would need to be performed to find the true limit of how flexible the wing tip feather could realistically be. If flight speed were slow enough, a highly flexible feather may truly mimic that of a bird and offer some amount of passive control. With some or all of these improvements, the wing tip feather could prove to be a way to increase efficiency in SUAS in the future.

8.2.2 Feather Layout and Wing Testing

While this research looked specifically to eagles and their wing shape as inspiration for the MFC feather wing, there are many different types of wings in the avian population. Avian wingtip shape has been explored extensively by Lockwood and Rayner in [25]. They present a wide range of wing shapes, even in just the subset of migratory birds. It could prove highly beneficial to study the wing tip shapes and their effects on feather efficiency.

One suggestion for furthering would be to study the effect of wing tip feather placement on induced drag and control authority, perhaps using computational fluid dynamics software such as Tornado or Athena Vortex Lattice (AVL). This may yield enlightening results regarding the optimum wing shape for non-flapping flight with wing tip feathers. After an optimization of the wing shape wind tunnel testing would be extremely advantageous for characterizing the effects of leading edge feathers on subsequent trailing feathers. These experiments would give great insight into actually implementing the tip feathers on real world SUAS.

8.2.3 Real World Wing Implementation

It would be enormously advantageous to perform experiments in which thes feathers operated on a real-world model. Such experiments would represent the ultimate realization of the MFC driven wing tip feather. Experiments and testing on a real world platform would give insight into how the MFC feathers impact endurance, and would also shed light on the feathers true control characteristics. The MFC feather has shown great promise in its initial development phase and could one day be implemented on a fixed wing aircraft, forever changing the way SUAS are designed in the future.

Bibliography

[1] J.-S. Park and J.-H. Kim, "Analytical development of single crystal macro fiber composite actuators for active twist rotor blades," *Smart Materials and Structures*, vol. 14, no. 4, pp. 745–753, 2005.

[2] S. M. Corp., "Macro fiber composite - mfc," 2003-2017. http://www.smart-material.com/MFC-product-main.html.

[3] O. J. O. III, B. M. David, S. L. Taylor, K. B. Kochersberger, T. Probst, P. A. Gelhausen, and J. Climer

[4] "Stability and control." University Lecture, 2008. Virginia Polytechnic Institute and State University.

[5] A. H. Bowers, O. J. Murillo, R. Jensen, B. Eslinger, and C. Gelzer, "On wings of minimum induced drag: Spanload implications for aircraft and birds," tech. rep., 2016.

[6] D.-K. Kim and J.-H. Han, "Smart flapping wing using macro-fiber composite actuators," *Smart Structures and Materials 2006: Smart Structures and Integrated Systems*, vol. 6173, no. 61730F, 2006.

[7] D.-K. Kim, J.-H. H. Hong-Il Kim, and K.-J. Kwon, "Experimental investigation on the aerodynamic characteristics of a bio-mimetic flapping wing with macro-fiber composites," *Journal of intelligent material systems and structures*, vol. 19, no. 3, pp. 423–431, 2008.

[8] M. A. Aldheeb, W. Asrar, E. Sulaeman, and A. A. Omar, "A review on aerodynamics of non-flapping bird wings," *SciELO Analytics*, vol. 8, no. 1, pp. 7–17, 2016.

[9] O. Bilgen, "Macro Fiber Composite Actuated Unmanned Air Vehicles: Design, Development, and Testing," Master's thesis, Virginia Polytechnic Institute and State University, 2007.

[10] Avid LLC., *Dual Channel MFC Bimorph High-Voltage Driver Technical Datasheet*, 12 2012.

[11] E. A. Gustafson, "Design, Simulation, and Wind Tunnel Verification of a Morphing Airfoil," Master's thesis, Virginia Polytechnic Institute and State University, 2011.

[12] P. C. Ltd., "Mechanical properties of carbon fibre composite materials, fibre / epoxy resin (120 c cure)." http://www.performance-composites.com/carbonfibre/mechanicalproperties_2.asp.

[13] T. A. Probst, "Evaluating the Aerodynamic Performance of MFC-Actuated Morphing Wings to Control a Small UAV," Master's thesis, Virginia Polytechnic Institute and State University, 2012.

[14] J. High, W. Wilkie, L. R. Center, and U. A. R. L. V. T. Directorate, *Method of Fabricating NASA-standard Macro-fiber Composite Piezoelectric Actuators*. NASA technical memorandum, National Aeronautics and Space Administration, Langley Research Center, 2003.

[15] B. R. Williams, D. J. Inman, M. R. Schultz, and M. W. Hyer, "Nonlinear tensile and shear behavior of macro fiber composite actuators," *Journal of Composite Materials*, vol. 38, no. 10, pp. 855–869, 2004.

[16] L. Prandtl, "Applications of modern hydrodynamics to aeronautics," tech. rep., 1979.

[17] T. A. Probst, K. Kochersberger, B. Stiltner, C. J. Hickling, O. J. O. I. E. Karni, C. Olien, and A. P. Blain, "Smart material actuators as a means of uav flight control," *50th AIAA Aerospace Sciences Meeting including the New Horizons Forum and Aerospace Exposition*, 2012.

[18] J. M. V. Rayner, "Form and function in avian flight," in *Current Ornithology* (R. F. Johnston, ed.), vol. 5, ch. 1, pp. 1–66, Springer US, 1988.

[19] E. Gustafson, *Learning FEMAP*. Independent Publisher, 2014.

[20] T. Merlin, "A vortex lattice matlab implementation for linear aerodynamic wing applications," Master's thesis, Royal Institute of Technology, 2000.

[21] Micro-Epsilon, *Betriebsanleitung Instruction Manual optoNCDT 1401*. X975x063-B020054MSC.

[22] National Instruments, *User Guide NI myDAQ*, 8 2014.

[23] W. J. Devenport and A. Borgoltz, "Experiment 3 - flow past a circular cylinder," 2016. www.dept.aoe.vt.edu/ aborgolt/aoe3054/manual/expt3/index.html.

[24] Micro-Epsilon, *Instruction Manual scanCONTROL 26xx*, 2008.

[25] R. Lockwood, J. P. Swaddle, and J. M. V. Rayner, "Avian wingtip shape reconsidered: wingtip shape indices and morphological adaptions to migration," *Journal of Avian Biology*, vol. 29, pp. 273–292, 1998.

[26] N. Hall, "Induced drag coefficient," 2015. www.grc.nasa.gov/www/k-12/airplane/induced.html.

Appendices

Appendix A

Wind Tunnel Uncertainty Measurements

This section describes the uncertainty measurements for the wind tunnel experiments. More specifically, this appendix shows an example calculation for the uncertainty in Reynold's number for a given trial. The uncertainty for the Reynolds number was calculated by taking the uncertainty in each base measurement and allowing that to propagate through the equations. The final uncertainty was a sum of the squares of all uncertainties derived from individual components (see Table A).

Table A.1: Sample calculations for the Reynolds number uncertainty measurement

Wind Tunnel Uncertainty					
Uncertainty in Density					
	Value	Uncertainty	A+dA,B	A,B+dB	
Primary Uncertainties					
Atmospheric Pressure	953.7	0.05	953.75	953.7	
Temperature	21.5	0.05	21.5	21.55	
Value					
Density	0.154557977		0.154566081	0.154199374	
		Difference	-8.10307E-06	0.000358603	
	Final Uncertainty	0.000358695			
Uncertainty in Kinematic Viscosity					
	Value	Uncertainty	A+dA,B	A,B+dB	
Primary Uncertainties					
Temperature	21.5	0.05	21.55	21.5	
Derived Uncertainties					
Dynamic Viscosity	1.10182E-06		1.10525E-06	1.10182E-06	
Density	0.154557977	0.000358695	0.154557977	0.154916672	
Value					
Kinematic Viscosity	7.12885E-06		7.15102E-06	7.11234E-06	
		Difference	-2.21718E-08	1.65062E-08	
	Final Uncertainty	2.76413E-08			
Uncertainty in Reynold's Number					
	Value	Uncertainty	A+dA,B,C	A,B+dB,C	A,B,C+dC
Primary Uncertainties					
Chord Length	0.035	0.005	0.04	0.035	0.035
Derived Uncertainties					
Free Stream Velocity	10.102	0.01	10.102	10.112	10.102
Kinematic Viscosity	7.12885E-06	2.76413E-08	7.12885E-06	7.12885E-06	7.15649E-06
Value					
Reynold's Number	49597.06697		56682.36225	49646.16325	49405.50289
		Difference	-7085.295281	-49.0962849	191.564074
	Final Uncertainty	7088.054491			

The final uncertianties for each trial were calculated in this way (see Table A).

Table A.2: Tabulated uncertainties of Reynolds number for each wind tunnel trial

Desired Velocity (m/s)	**Free Stream Velocity (m/s)**	**Reynolds Number**	**Uncertainty**
10	10.10	49600	7100
15	15.11	70300	10000
20	10.06	88500	12700
25	24.77	114000	16300

Appendix B

Laser Rangefinder Calibration

The laser rangefinder used in all physical experiments, the Micro-Epsilon optoNCDT1401, outputs a electrical current proportional to distance measured. This current was measured in the experiment by the myDAQ, but the relationship between the distance and current still needed to be determined. To calculate the linear equation the laser rangefinder was used to measure two known distances of 60 mm and 260 mm (see Figure B.1). These two known distances were chosen as they defined the outer reaches of the range of the rangefinder. To verify the relationship a point at 100 mm was then measured and compared to the equation found.

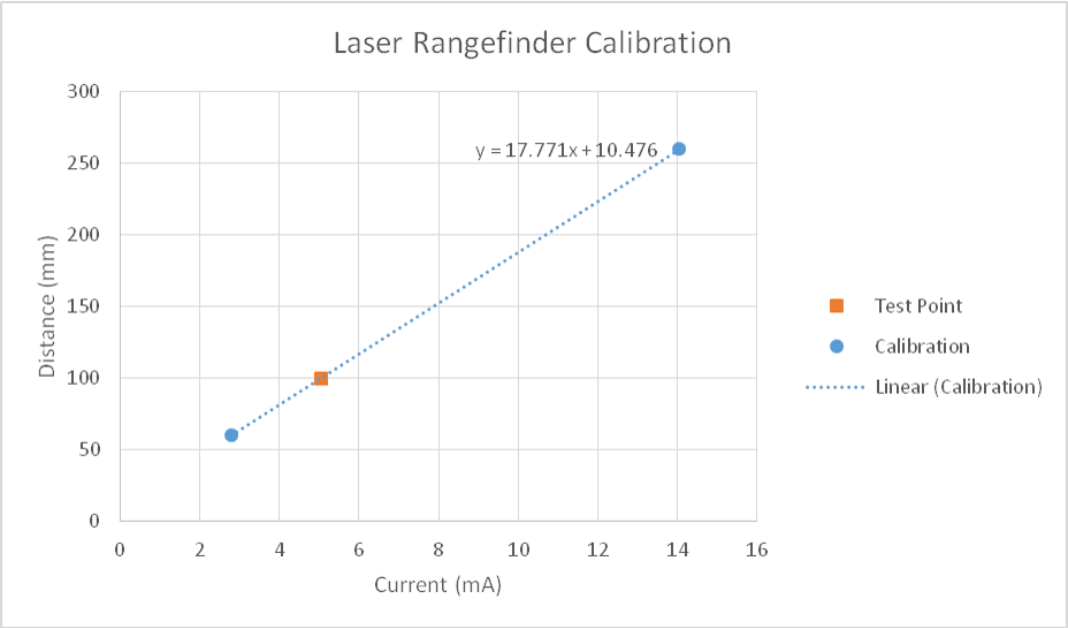

Figure B.1: Laser rangefinder linear calibration

The two calibration points yielded a linear equation of the model $y = mx + b$, where x is the current measured and y is the distance. The equation came out to be $m = 17.77149$ and $b = 10.47583$. The verification point, when measured and plugged into the equation, yielding a calculated distance of 100.1008mm. So the relationship was confirmed linear with an error of 0.1%. This error was acceptable for the precision required for all experiments.